Impact of aluminium and gallium substitutions on the ferrihydrite and goethite structure: Consequences for rare earth element adsorption and complexation

Anne Buist, Camille Rivard, Mélanie Davranche, François Brisset, Khalil Hanna, Erwan Paineau, Stéphan Rouzière, Erik Elkaim, Stéphanie Blanchandin, Karine Chaouchi, et al.

Chemical Geology 667 (2024) 122312

Contents lists available at ScienceDirect

Chemical Geology

journal homepage: www.elsevier.com/locate/chemgeo

Impact of aluminium and gallium substitutions on the ferrihydrite and goethite structure: Consequences for rare earth element adsorption and complexation

Anne Buist [a,*], Camille Rivard [a,b], Mélanie Davranche [c], Francois Brisset [d], Khalil Hanna [e], Erwan Paineau [f], Stéphan Rouzière [f], Erik Elkaim [a], Stéphanie Blanchandin [a], Karine Chaouchi [a], Claire Hotton [f], Aline Dia [c], Delphine Vantelon [a]

[a] Synchrotron SOLEIL, L'Orme des merisiers, Départementale 128, 91190 Saint-Aubin, France
[b] INRAE, TRANSFORM, 44300 Nantes, France
[c] Univ Rennes, CNRS, Géosciences Rennes – UMR 6118, F-35000 Rennes, France
[d] Institut Chimie Moléculaire et des Matériaux d'Orsay, UMR CNRS 8182, Université Paris-Saclay, 17 Avenue des Sciences, Bâtiment 670, 91405 Orsay, France
[e] Ecole Nationale Supérieure de Chimie de Rennes, UMR CNRS 6226, 11 Allée de Beaulieu, Université de Rennes, 35708 Rennes, France
[f] Laboratoire de Physique des Solides, UMR CNRS 8502, Université Paris-Saclay, 1 rue Nicolas Appert, Bâtiment 510, 91405 Orsay, France

ARTICLE INFO

Editor: Oleg Pokrovsky

Keywords:
Rare earth elements
Adsorption
iron (oxy)hydroxides
Al substitution
Ga substitution
Nd speciation
EXAFS

ABSTRACT

The increase in use and extraction of Rare Earth Element (REE) over the last few decades has raised concerns about their behaviour in the environment. One of the factors controlling their fate is adsorption onto iron (Fe) (oxy)hydroxides. In natural systems, aluminium (Al) substitutions of iron often occur in these (oxy)hydroxides, as Al is also one of the most abundant elements at the Earth's surface. Though it has been shown that these substitutions can have an impact on the adsorption of different metallic contaminants, to date, no study has been carried out on the impact of substitution on the adsorption of REE.

To fill this gap, a series of ferrihydrites and goethites with varying levels of Al and gallium (Ga) substitution were synthesized, with Ga used as it is a chemical analogue of Al with an ionic radius comparable to that of Fe, unlike Al whose radius is smaller. The synthetised (oxy)hydroxides were subjected to REE adsorption at acidic to near neutral pH. REE complexation modes were studied using EXAFS collected at the neodymium L_3-edge. Results show that the amount of adsorbed REE is controlled both by the pH of solution and the structure of the adsorbing (oxy)hydroxide. Adsorbed REE form both bidentate mononuclear (BM) and bidentate binuclear (BB) complexes. Unlike goethite, in the ferrihydrite the substitution affects the size, shape and organisation of the surface sites of the particle. The number of sites allowing BM complexation decrease with increasing substitution, as Al and Ga inhibit the protrusion of metal octahedra at the (1−10) plane. Additionally, Al substitution inhibits the growth of the step wise (1−1−1) plane and its reciprocals, leading to the particle shape changing from spherical to cylindrical and a loss of adsorption sites capable of forming both BM and BB complexes.

With this study we demonstrate that the substitution of Fe by Al and Ga in goethite has little to no effect, while in the ferrihydrite it leads to a modification in particle shape, accompanied by a reduction in adsorption sites, resulting in a decrease in total adsorption. Consequently, contrary to goethite, substitution in ferrihydrite strongly reduces its capacity to trap and transport REE.

1. Introduction

Rare Earth Elements (REE) are defined as a group of 17 elements, comprised of scandium (Sc), yttrium (Y), and the 15 lanthanides (Ln), by the International Union of Pure and Applied Chemistry (IUPAC). With the discovery of their unique magnetic and electrical properties, the use and application of REE have grown over the last decades and they are currently considered indispensable for the ever-growing technology and renewable energy sector (Castor and Hedrick, 2006; Haque et al., 2014; Wall, 2014). To keep up with growing demand, there has been a

* Corresponding author at: SOLEIL Synchrotron. L'Orme des Merisiers, Départementale 128, 91190 Saint-Aubin, France.
E-mail address: delphine.vantelon@synchrotron-soleil.fr (D. Vantelon).

https://doi.org/10.1016/j.chemgeo.2024.122312
Received 27 February 2024; Received in revised form 8 July 2024; Accepted 7 August 2024
Available online 8 August 2024

four-fold increase in REE production by mines (U.S. Geological Survey, 1996; U.S. Geological Survey, 2022). With this increase in REE consumption, higher concentrations of all REE have been measured in rivers and soils near mining areas and in areas where REE fertilizers were used (Liang et al., 2014; Otero et al., 2005; Tyler, 2004). Anomalously high concentrations of individual REE have also been found in rivers and have been traced to either medical or industrial waste streams (Bau and Dulski, 1996; Hatje et al., 2016; Inoue et al., 2020; Klaver et al., 2014; Kulaksız and Bau, 2013).

With ever-increasing levels of anthropogenic REE in soils and surface waters, concerns about REE behaviour in the environment and its effect on living organisms are also rising. Recent studies reveal that exposure to REE exceeding natural levels have negative effects on ecosystems and human health (Brouziotis et al., 2022; Egler et al., 2022; Gwenzi et al., 2018; Pagano et al., 2019; Revel et al., 2023) while their behaviour in the environment, and in particular their transfer processes, have yet to be fully characterized (Gwenzi et al., 2018; Hissler et al., 2023; Tyler, 2004).

In natural aqueous surface and subsurface systems, colloids are known to play a major role in the mobility of metallic pollutants, including REE (Dia et al., 2000; Kretzschmar and Schafer, 2005). Colloids are described as nanometric particles with a high density of reactive surface sites and specific surface area, which can consist of both minerals (i.e. metallic oxides, clays) and organic material. One of the most studied inorganic colloids is ferrihydrite (Fh), a poorly crystalline iron (Fe) hydroxide that is widespread in near-surface environments and whose role in the behaviour of trace metals has repeatedly been demonstrated (Jambor and Dutrizac, 1998; Schwertmann and Taylor, 1989). REE complexation with natural ferrihydrite and goethite (Goe), a thermodynamically stable transformation product of Fh, has also been reported (Bau, 1999; Compton et al., 2003; Ratié et al., 2020; Santofimia et al., 2022). At the same time, laboratory experiments have demonstrated that various environmental parameters can modify REE adsorption on Fe (oxy)hydroxides, such as the nature of the phase, the presence of organic matter or carbonates as well as the pH, temperature, and ionic strength (Davranche et al., 2004; Quinn et al., 2006a, 2006b, 2007).

However, in natural systems Fe (oxy)hydroxides often contain metal impurities such as aluminium (Al) as Al is one of the most abundant elements at the Earth's surface that is known to substitute for Fe in Fe (oxy)hydroxides structures. The impact of such substitutions on the adsorption capacity of Fe (oxy)hydroxides has already been studied for various oxyanions and metals (Adra et al., 2016; Cismasu et al., 2013; Liang et al., 2021, 2022; Ma et al., 2015; Ni et al., 2016, 2017; Souza et al., 2021). In general, these studies have shown that substitution enhances the adsorption capacity of (oxy)hydroxides for both oxyanions and metal cations. However, Cismasu et al. (2013) shows that, at low adsorbate concentrations, pure Fh adsorbs as much as Al substituted Fh. To our knowledge, no study has been performed on the effect of substitution in Fe-(oxy)hydroxide structures, on adsorption of REE.

The goal of this study is to determine if substitutions in Fe (oxy) hydroxides help or hinder the removal of REE from solution. For this purpose, a series of Fh and Goe with varying levels of Al as well as gallium (Ga) were synthetised. As previously mentioned, Al-substitution in Fe (oxy)hydroxides is common in natural systems. As for gallium, it is often found to coexist with REE and other critical elements in mine wastes (e.g. pyrite or coal) (Cánovas et al., 2021; Dai et al., 2012; Zou et al., 2017) and it is used together with REE in smartphone technology (Bookhagen et al., 2020) and LEDs (De Oliveira et al., 2021). Furthermore, Ga and Al have a similar chemistry in solution (Bradley et al., 1990), though their different ionic radii (Al^{3+} at 0.535 Å vs Ga^{3+} at 0.620 Å as compared to the Fe^{3+} one (0.645 Å) (Shannon, 1976)) may induce variable structural distortions of the substituted Fe (oxy) hydroxides.

The synthesized (oxy)hydroxides were first analysed to determine whether Al and Ga were incorporated into the structure, and how this modified size and shape, and surface properties of the particles. Subsequently, adsorption experiments were carried out on all REE at variable pH to study the effect of pH and the nature of the (oxy)hydroxides on their adsorption capacity. Finally, neodymium (Nd) was chosen as a proxy for all REE to look at the REE binding modes at the (oxy)hydroxide surface, as the differences in electron configuration between the REE, i.e. the filling of the 4f sub-shell, has no impact on their chemical behaviour due to the 4f electrons being shielded from chemical interactions by the $5s^2$ and $5p^6$ sub-shells (Henderson, 1984). Neodymium was adsorbed on all the (oxy)hydroxides and its binding modes were characterized by extended X-ray absorption fine structure (EXAFS) spectroscopy performed at the L_3-edge of Nd.

2. Methods and materials

2.1. Synthesis of the metal (oxy)hydroxide series

The substituted goethite and ferrihydrite series were synthesized following the protocols described by Schwertmann and Cornell (2000) and detailed in the following paragraphs. All aqueous solutions were prepared with ultrapure water (milli-Q-Integral, Millipore). Elemental content in the final solid phases was determined by ICP-OES (Al & Fe) and ICP-MS (Ga & REE) by the Service d'Analyse des Roches et Minéraux (SARM, Nancy). These results (Tables S1 to S3 of the supplementary information) were used to calculate the final Al/(Al + Fe) and Ga/(Ga + Fe) substitution ratios.

2.1.1. Synthesis of substituted goethite

Solutions of 1 M $Fe(NO_3)_3 \bullet 9H_2O$, and 0.5 M of $Al(NO_3)_3 \bullet 9H_2O$ and $Ga(NO_3)_3 \bullet 9H_2O$ (99% pure, Sigma Aldrich) were mixed in varying ratios (Table 1) with 5 M KOH to reach pH 11.7, before being topped up to 2 L with ultrapure water. These suspensions were aged in an oven for 14 days at 70 °C, shaking the bottle once a day. The precipitates were then washed twice with 300 mL of 1 M KOH and centrifuged at 8888*g* for 30 min, before adjusting the pH to 7.5 with 1 M HCl and washing one last time with ultrapure water. Lastly, the precipitates were dried in a glass crystallising dish at room temperature and crushed with an agate mortar and pestle for storage. Resulting in pure Goe, Al/(Al + Fe) ratios of 4.3 (Goe4.5Al), and 9.0 (Goe9Al), and Ga/(Ga + Fe) ratios of 3.3 (Goe3.5Ga), and 6.3 (Goe7Ga).

2.1.2. Synthesis of substituted ferrihydrite

Solutions of 0.2 M of $Fe(NO_3)_3 \bullet 9H_2O$, $Al(NO_3)_3 \bullet 9H_2O$, and $Ga(NO_3)_3 \bullet 9H_2O$ were combined to achieve a total volume of 500 mL, using solution ratios reported in Table 1 to obtain final ratios of Al/(Al + Fe) or Ga/(Ga + Fe) equal to 0 (Fh), 10 (Fh10Ga), 20 (Fh20Al and Fh20Ga), 34 (Fh35Al), and 100 (AlO(OH) and GaO(OH)) in the solid ferrihydrite series.

The solid precipitates were obtained by titrating the solutions to pH 7 using 1 M KOH, except for the Fh35Al and poorly crystalline Al (oxy) hydroxide (AlO(OH)), which were titrated to pH 5 to prevent crystallisation. To accelerate the co-precipitation of Fe and Al/Ga, 250 mL of 1 M KOH was added at once before titrating to pH 7. The precipitates were washed three times using ultrapure water and centrifuged at 8888*g* for 30 min. Lastly, the precipitates were dried in a crystallising dish at room temperature and crushed for storage. Note that the crystallinity of GaO (OH) could not be reduced, even when limiting the pH to 5, as the precipitate always turned into a crystalline X-ray diffracting α-GaO(OH).

2.2. Characterisation of the Fe, Al, and Ga (oxy)hydroxides

The point of zero charge (PZC) was determined by performing potentiometric titrations at the Ecole Supérieure de Chimie (ENSC) in Rennes. First, 0.1 g of synthesized (oxy)hydroxide was added to 100 mL of NaCl at different ionic strengths (10^{-3}, 10^{-2}, and 10^{-1} mol L^{-1}) under N_2 atmosphere. Before each titration, CO_2 was removed from the

Table 1
Concentration (in mol L^{-1}) and volume (in mL) of solution used for the synthesis of the metal (oxy)hydroxides, and their substitution ratio in percentage. The substitution ratio in Al/(Al + Fe) or Ga/(Ga + Fe) was calculated from the metal concentrations in the final solid phases.

Chemical	Conc.	Goe	Goe4.5Al	Goe9Al	Goe3.5Ga	Goe7Ga
$Fe(NO_3)_3 \bullet 9H_2O$	1	100	100	100	100	100
$Al(NO_3)_3 \bullet 9H_2O$	0.5	–	50	120	–	–
$Ga(NO_3)_3 \bullet 9H_2O$	0.5	–	–	–	50	120
KOH	5	180	174	165	174	165
Substitution ratio (in %)		–	4.3	9.0	3.3	6.3

	Conc.	Fh	Fh20Al	Fh35Al	Fh10Ga	Fh20Ga	Al O(OH)	Ga O(OH)
$Fe(NO_3)_3 \bullet 9H_2O$	0.2	500	400	300	450	400	–	–
$Al(NO_3)_3 \bullet 9H_2O$	0.2	–	100	200	–	–	500	–
$Ga(NO_3)_3 \bullet 9H_2O$	0.2	–	–	–	50	100	–	500
Substitution ratio (in %)		–	20	34	10	20	–	–

suspensions by purging with N_2 gas in a double-walled Pyrex cell, kept at a constant temperature by use of a thermostat.

The pH of suspension was monitored using a combined glass electrode (Orion pH meter model 710 A) and adjusted with solutions of 1 M HCl and 1 M NaOH.

The shape and size of the synthesized Fe/Al/Ga (oxy)hydroxides were observed using a transmission electron microscope (TEM) (JEOL JEM-2100 plus) at the Université Paris-Saclay. For these measurements, ~1 mg of Fe/Al/Ga (oxy)hydroxide was suspended in ~2 mL ethanol (96% vol., VWR chemicals) and shaken until homogenous. A drop of this suspension was deposited on a carbon coated copper grid, with the ethanol evaporating and the particles settling on the grid.

The specific surface area (SSA) was determined by N_2 adsorption-desorption using the Brunauer-Emmet-Teller (BET) model, performed at the Institute des Sciences Chimiques de Rennes (ISCR). To overcome the effects of surface hydration, the (oxy)hydroxide powders were first outgassed under vacuum at 150 °C. After which N_2 physisorption was done with a Micromeritics Gemini VII 2390 t, using a gas mixture of N_2/He (30/70).

The crystallinity of the Fe (oxy)hydroxide phases, and the effect of substitution on the lattice, was observed by X-ray diffraction measurements performed with the two-circle powder diffractometer equipped with silicon-strip linear detectors (Mythen2, Dectris) on the CRISTAL beamline (Itie et al., 2012) at the SOLEIL synchrotron (Saint Aubin, France). The wavelength was $\lambda = 0.051427$ nm for the ferrihydrite series and $\lambda = 0.07287$ nm for the goethite series measurements. The powders were put into glass capillaries with a diameter of 0.1 mm and measurements were performed over a 2θ range of 30°, with steps of 1° and a counting time of 5 s per step.

For the goethite series the space group and lattice parameters were refined and extracted through whole pattern profile matching (Figs. S1-S5), using the Le Bail method in the FullProf software (Rodriguez-Carvajal, 1990).

The Al and Ga (oxy)hydroxides (AlO(OH) and GaO(OH)) were measured using a D2-phaser X-Ray Diffractometer (Bruker) equipped with a Cu-Kα X-Ray tube generator ($\lambda = 0.15418$ nm) at SOLEIL synchrotron. The measurements were performed on powder with a flattened surface, over a 2θ angle range of 10°-60°, with steps of 0.02° 2θ and a counting time of 1 s per step.

The domains of coherency in the ferrihydrite series were determined using Pair Distribution Function (PDF) measurements performed at the CRISTAL beamline, using the same sample environment set-up as the XRD measurements. The measurements were performed at a wavelength of $\lambda = 0.051427$ nm, over 85 steps, with the step size decreasing from 2° to 0.5° with the increase of the angle, and a counting time of 20 s per step.

The hydration rate, and the temperature of dehydration, dehydroxylation, and phase transition of the ferrihydrite series were determined using Thermogravimetric and Differential Thermal Analysis (TG/DTA) measurements, performed on a LabSys evo from Setaram at SOLEIL synchrotron. An Al_2O_3 crucible was filled with 65 mg (oxy)hydroxide powder and placed in the instrument alongside an empty reference crucible. The oven increased the temperature from 30 °C to 1000 °C in 5 °C /min increments. Once 1000 °C was reached the temperature was maintained for 10 min before cooling back down to 30 °C at 5 °C /min. This was all done under a flow of dry air (20 mL min^{-1}).

The results from these measurements were used to calculate the loss of H_2O and OH in weight percent (wt%). The loss of H_2O was calculated in comparison to the initial weight of the sample, while the loss of OH was calculated in comparison to the initial weight minus the weight lost during dehydration.

2.3. Rare earth element pH-edge adsorption experiments

The pH-edge experiments were performed in 100 mL milliQ water in which 100 µL of 1 M NaCl, 20 µL of 100 mg L^{-1} REE stock solution (comprised of the lanthanides, Sc, Y, Th, and U, Inorganic Ventures), and 15 mg of (oxy)hydroxide powder was added. To obtain the pH range, from 3 to 7 for the goethite series and GaO(OH) and 4.5–7 for the ferrihydrite series and AlO(OH), the pH of the suspension was adjusted with NaOH solutions of 0.1, 0.01, and 0.001 M for pH ≥ 4, and 0.1 M of HNO_3 to obtain pH 3. According to stability diagrams of the different REE, at these concentrations, at pH ≤ 7, and at equilibrium with the atmosphere, all REE are present in their ionic form. No precipitation occurs except for the cerium (Ce), which may partly precipitate when oxidised to its 4+ oxidation state at pH ≥ 6 (Brookins, 1983; Ratié et al., 2023).

Each experiment was performed in triplicate. For the crystalline goethite series, and GaO(OH), the pH was adjusted between the addition of REE and that of the (oxy)hydroxide. Hereafter, the goethite suspensions were agitated on a shake plate for 48 h with no further pH monitoring.

For the poorly crystalline ferrihydrite series, and AlO(OH), the (oxy) hydroxide was added to the solution first and left on the shake plate overnight, before the REE stock solution was added. Once everything was in solution the pH was adjusted and the suspensions were agitated for 48 h, with two pH adjustments in the first 24 h. These adjustments to the protocol were made, as the pH of the poorly crystalline suspensions was more unstable and without these pH adjustments the pH at the end of adsorption would not exceed 5.

After 48 h, the end pH was measured, and a 10 mL sample of the suspension was taken and filtered using a 0.2 µm cellulose acetate filter (Sartorius). The filtered samples were acidified using 14.6 N HNO_3 and diluted with 0.37 N HNO_3 to determine the REE concentration with a Quadrupole ICP-MS (Agilent Technologies 7700 ICP-MS, Université de Rennes 1) (Tables S4 to S15).

For the ICP-MS measurements, a conventional calibration procedure with multi-elemental solutions was used, with the calibration solutions acidified to 2% nitric acid (HNO_3) and concentrations between 0.005 and 2 μg L^{-1}. Instrumental drift was corrected, reproducibility was checked, and the limit of detection and isobaric interferences were calculated (Davranche et al., 2004). The uncertainties for all trace elements are below ±5%.

2.4. Neodymium adsorption experiments

The neodymium (Nd) adsorption was performed based on the protocol used in Ratié et al. (2023), using a 200 mL solution of 1 mM L^{-1} NaCl, 1000 μg L^{-1} of Nd, and 100 mg of (oxy)hydroxide powder. This change from the pH edge conditions is necessary, to obtain enough solids to prepare pellets for the XAS measurements, and to obtain a better signal to allow for good EXAFS fits. For the pure goethite an additional run was done with 200 μg L^{-1} of Nd, to differentiate the Goe they will be denoted as 1000-Goe and 200-Goe from here on out. The pH of solution was adjusted to 7 to ensure high amounts of adsorption, using the same NaOH solutions used for the pH-edge experiment. According to the Nd stability diagram Nd is expected to remain soluble in solution, even at the higher concentrations than the ones used for the pH edge experiments, at pH = 7 and in equilibrium with the atmosphere. No precipitate is expected to have formed (Brookins, 1983; Ratié et al., 2023).

As with the pH-edge experiments the protocol for the ferrihydrite series and AlO(OH) differs from that for the goethite series and GaO(OH). For the goethites and GaO(OH), the Nd was added before the pH was adjusted to 7 and the (oxy)hydroxides were added. For the ferrihydrites and AlO(OH) the (oxy)hydroxide was added 24 h before the Nd, and the pH was adjusted with both in solution.

The subsequent suspensions were agitated on a shake plate for 48 h, and the pH of the poorly crystalline (oxy)hydroxide suspensions were adjusted twice during the first 24 h. After agitation, a 10 mL sample of the suspension was filtered for ICP-MS measurements to determine the amount of Nd adsorbed. The rest of the suspension was centrifuged for 30 min at 1550*g* and air dried in the centrifuge tube. Once dry the precipitate was crushed and stored as a powder.

2.5. Neodymium L_3-edge extended X-ray absorption fine structure (EXAFS)

The L_3-edge Nd EXAFS was measured on the LUCIA beamline of SOLEIL synchrotron (Flank et al., 2006; Vantelon et al., 2016), using a Si (111) double-crystal monochromator. During the measurements the samples were kept under a secondary vacuum (10^{-7} mbar) and at 80 K using a He cryostat. The EXAFS measurements were performed on 10 mm diameter pellets made from a homogeneous mixture of 35 mg of metal (oxy)hydroxide powder and 5 mg of cellulose. The data was obtained in fluorescence mode, using a Bruker 60 mm^2 mono-element SDD that was at an angle of 25° in relation to the sample surface. The Nd_2O_3 reference pellet was prepared as a homogeneous mixture of 3 mg Nd_2O_3 (Sigma Aldrich) and 32 mg of cellulose and measured in transmission mode using a Si diode detector.

In the pre-peak region (6100–6190 eV) the spectra were collected with a step-size and a counting time of 2 eV and 1 s. The edge region (6190–6270 eV) was scanned with a step size and a counting time of 0.2 eV and 1 s. The EXAFS region (6270–6710 eV) was scanned with a step size increasing from 0.5 to 2 eV and a counting time of 1 to 3 s. Six to18 spectra were merged for analysis.

The Nd spectra were normalized and extracted using the ATHENA software (Ravel and Newville, 2005) including the Autbk algorithm (Rbkg = 1, k-weight = 3). Normalized spectra were obtained by fitting the pre-edge and post-edge regions with a linear and a quadratic polynomial function, respectively. The Fourier Transform (FT) of the k^3-weighted EXAFS spectra was calculated over a range of 2.7–9.5 $Å^{-1}$ using a Hanning apodization window (window parameter = 1). EXAFS fitting was performed in the 1.3–4.4 Å distance range with the ARTEMIS (Ravel and Newville, 2005) interface using the IFEFFIT least-squares refinements. Paths used for fitting were calculated from a $Nd_3Fe_5O_{12}$ garnet structure (Komori et al., 2009) using the FEFF6 algorithm included in the ARTEMIS interface.

The S_0^2 and ΔE parameters were extracted from the fit calculation of the Nd_2O_3 reference (Fig. S6, Table S16).

3. Results & discussion

3.1. Absence of modification of Fe (oxy)hydroxide phases resulting from Al and Ga substitution

The diffractogram of goethite (Fig. 1A) is consistent with those found in literature (Schwertmann and Cornell, 2000). Despite the low rate of substitution, the introduction of Al in goethite leads to a shift of the peaks to smaller distances with increasing Al content, as well as an increase in intensity for some of the peaks, similar to observations reported by Liang et al. (2021). The Ga substitution also shifts the peaks compared to pure Goe, though less pronounced than for the Al-substitution, while no peak intensity differences were observed. These results can be related to the difference between the ionic radius of Fe^{3+} (0.645 Å) versus Al^{3+} (0.535 Å) and Ga^{3+} (0.620 Å) (Shannon, 1976), with the greater decrease in ionic radius from Fe^{3+} to Al^{3+} than Fe^{3+} to Ga^{3+}, having a greater effect on the crystal lattice. This is confirmed by whole profile pattern matching (Figs. S1-S5), which has shown that the volume of the unit cell and the a, b, and c parameters decrease with increasing substitutions of both Al and Ga (Table 2). With the Al generally causing a larger decrease, except for in the c parameter on which Al and Ga have the same effect.

The diffractogram of the GaO(OH) (Fig. 1B) demonstrates the formation of a crystalline α-GaO(OH) phase, showing multiple peaks in a pattern consistent with the XRD results of Taş et al. (2002). On the other hand, the AlO(OH) diffractogram (Fig. 1B) shows a nearly flat line with only two small broad 'peaks' due to its poorly crystalline nature and nano-size.

The diffractograms of the ferrihydrites (Fig. 1C) show two broad peaks in line with 2-line ferrihydrite diffractograms (Schwertmann and Cornell, 2000). Both Al and Ga substitution promote peak broadening and a decrease in intensity, with the Al substitution resulting in the broadest peaks and the Ga substitution in the lowest intensity peaks. This was also observed in Al substituted Fh by Cismasu et al. (2012) and Adra et al. (2016). Neither the Al, nor the Ga, substituted ferrihydrite diffractograms show additional structures that would reveal the presence of additional phases. This is in agreement with theoretical Helmholtz free energy calculations that show a maximum of 35% Al substitution in Fh (Guimarães Jr et al., 2023).

In both the goethite and the ferrihydrite series, the XRD patterns reveal that Al and Ga enter the structure and no additional phase is observable.

3.2. Impact of Al and Ga substitution on the structural hydroxyls and water content

The pH_{PZC} for the goethite series, ranging from 8.3 to 8.6 ± 0.1, is not affected by the substitution as previously observed by Liang et al. (2021) (Table 3). In contrast, the pH_{PZC} of the Al and Ga (oxy)hydroxide reached 8.7 ± 0.1 for GaO(OH), and 9.4 ± 0.1 for AlO(OH). The pH_{PZC} of the pure Fh is the lowest of all the (oxy)hydroxides with pH_{PZC} = 7.9 ± 0.1. All these pH_{PZC} values are within the range of the values reported in the review made by Komulski (Kosmulski, 2018). The increase in substitution rate increases the pH_{PZC} until 8.8 ± 0.1 for Fh35Al. The lower pH_{PZC} of Fh compared to Goe, as well as the increase of pH_{PZC} with Al substitution in Fh, was previously observed by several authors and is within the pH_{PZC} range of 7.6 to 9 for pure up to 24% Al substitution Fh

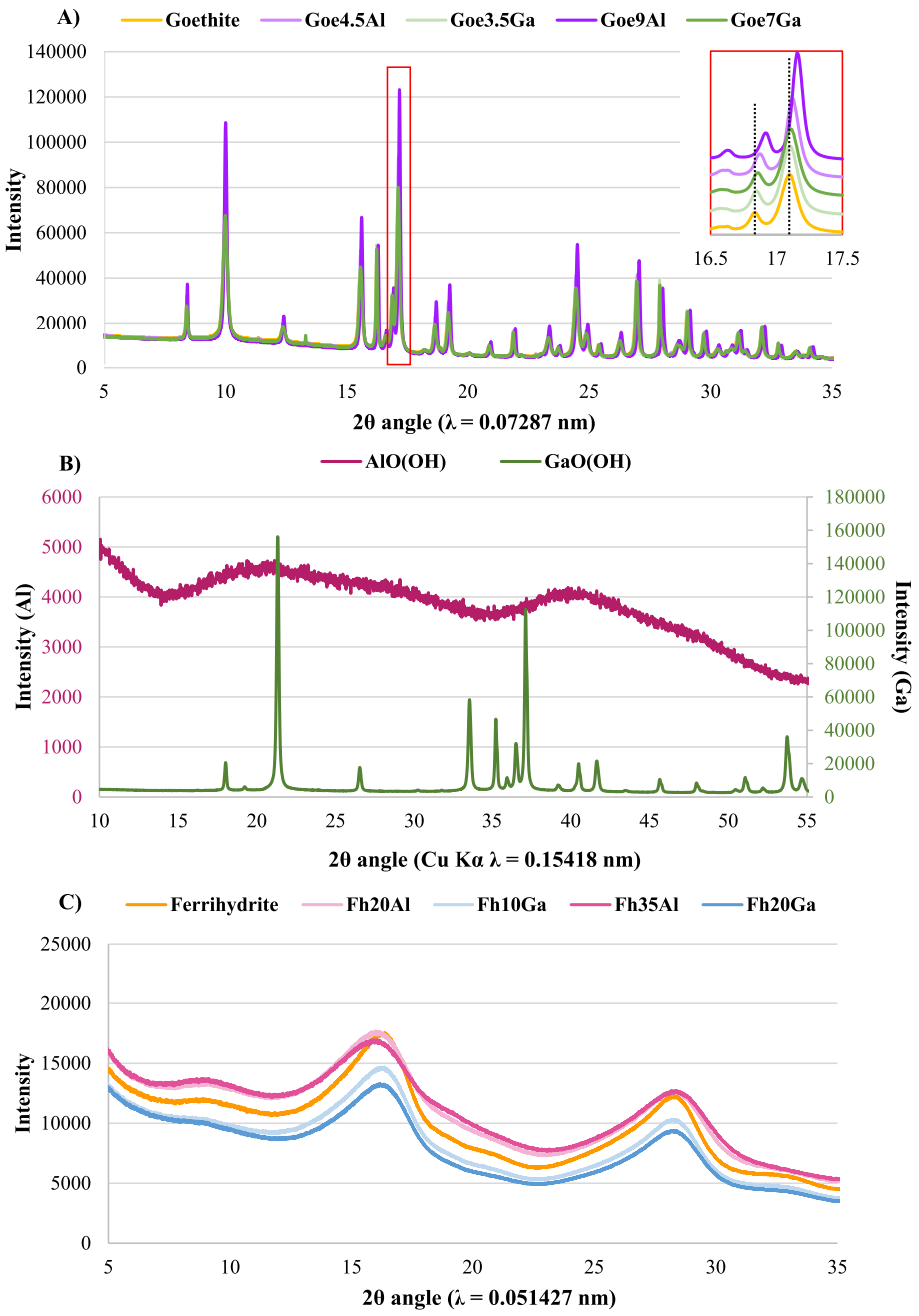

Fig. 1. X-Ray Diffractograms of A) the goethite series and C) the ferrihydrite series, measured at the CRISTAL beamline, and B) AlO(OH), and GaO(OH) measured with a D2-phaser Bruker XRD equipped with a Cu source. In the box in A) the diffractograms are vertically stacked for better visualization; the dotted lines at 16.84 and 17.09° 2θ indicate the angular shift.

Table 2
Unit cell parameters for the pure and substituted goethites, obtained through whole profile pattern matching.

	Goe	Goe4.5Al	Goe9Al	Goe3.5Ga	Goe7Ga
a (Å)	9.9561	9.9357	9.9204	9.9467	9.9407
b (Å)	3.0230	3.0177	3.0117	3.0222	3.0211
c (Å)	4.6130	4.6102	4.6081	4.6096	4.6070
Volume (Å^2)	138.84	138.22	137.68	138.57	138.36

reported (Masue et al., 2007; Cismasu et al., 2013; Namayandeh and Kabengi, 2019; Liang et al., 2022). According to Liang et al. (2022), the slight increase of Fh pH_{PZC} with increasing Al content is due to the $\log K_H$ difference between Fe–OH and Al-OH sites. However, note that in our study the increase in pH_{PZC} is not linearly correlated with the increase in substitution rate.

The DTA curves of the ferrihydrite series (Fig. 2A) show two endothermal reactions, one at 115–130 °C related to dehydration and one between 325 and 390 °C related to dehydroxylation, and one exothermal peak related to phase transition (Carta et al., 2009). The dehydroxylation peak is not visible in the pure Fh data as it coincides with the positive exothermal peak. As in the XRD patterns, the shift of the phase transition to higher temperature with higher substitution rates demonstrates that Al and Ga are incorporated in the ferrihydrite structure. Meanwhile, the absence of a second exothermal peak around 837 °C for the Al substituted ferrihydrites, or 726 °C for the Ga substituted ferrihydrites, indicates the absence of secondary AlO(OH) or GaO(OH) phases.

Table 3
pH point of zero charge (pHpzc) and specific surface area (SSA), of the pure and substituted goethite and ferrihydrite, AlO(OH), and GaO(OH).

	Goe	Goe4.5Al	Goe9Al	Goe3.5Ga	Goe7Ga	GaO (OH)
pH_{pzc}	8.4 ± 0.1	8.3 ± 0.1	8.4 ± 0.1	8.6 ± 0.1	8.5 ± 0.1	8.7 ± 0.1
SSA (m^2 g^{-1})	37.1 ± 0.1	39.6 ± 0.1	30.7 ± 0.2	43.9 ± 0.2	39.9 ± 0.2	5.56 ± 0.01

	Fh	Fh20Al	Fh35Al	Fh10Ga	Fh20Ga	AlO(OH)
pH_{pzc}	7.9 ± 0.1	8.4 ± 0.1	8.8 ± 0.1	8.3 ± 0.1	8.6 ± 0.1	9.4 ± 0.1
SSA (m^2 g^{-1})	322 ± 1	308 ± 3	198 ± 4	338 ± 1	284 ± 4	2.63 ± 0.01

The H_2O and OH contents of each phase were calculated from the thermogravimetric analysis (Fig. 2B) and reported in Table 4. The H_2O content of the ferrihydrite series ranges from 20 to 28 wt%, with no clear trend in the effect of substitution on the hydration and the AlO(OH) contains the highest weight percent of water at 33%. On the contrary, while the OH content is stable for the Ga substitution at 3.0–3.5 wt%, the OH increases with the Al substitution rate from 3.5 for Fh to 6, 10, and 27 wt% for Fh20Al, Fh35Al, and AlO(OH) respectively.

3.3. The effect of Al and Ga substitution on the Fe (oxy)hydroxide morphology, size, and specific surface area

The TEM images of the goethites (Fig. S7A-E) show that the particles display an acicular shape. The particle size varies from 20 to 150 nm in width and from 0.1 to 1 μm in length and is consistent with the literature (Livi et al., 2017). Differences in shape according to amount of substitution in the goethites are negligible. However, the Goe9Al exhibits an aspect ratio (width-to-length) of 0.2 compared to the aspect ratio of 0.1 of the other goethites. Xu et al. (2019) and Liang et al. (2021) reported a similar change in aspect ratio of Goe with Al substitution. The SSA of the goethites vary from 37.1 ± 0.1 to 43.9 ± 0.2 m^2 g^{-1}, which is higher than the Goe9Al SSA of 30.7 ± 0.2 m^2 g^{-1} and above the range of 20–30 m^2 g^{-1} described by Schwertmann and Cornell (2000). No relation was found between the amount of substitution and the variation in SSA.

The GaO(OH) has a more tabular habit and is much larger than the needles in the goethite series, with an average size of ~300 × 550 nm (Fig. S7F). This is consistent with its small SSA of 5.56 ± 0.01 m^2 g^{-1} (Table 3), and with the size and shape observed at room temperature when using a hydrothermal synthesis method (Reddy et al., 2015).

The ferrihydrite and AlO(OH) particles (Fig. S8A—F) show aggregates from which individual particles cannot be distinguished. The size of the aggregates varies from 50 nm to 2.5 μm. AlO(OH) has the smallest SSA of the (oxy)hydroxides studied, 2.63 ± 0.01 m^2 g^{-1}, slightly lower than the SSA of GaO(OH) (Table 3). The SSA of the ferrihydrites vary from 198 to 338 m^2 g^{-1}, similar to the 200 to 320 m^2 g^{-1} range observed by Schwertmann and Cornell (2000), and it decreases with the increase of Al substitution (Table 3). This decrease in SSA with increasing Al content was also observed by Cismasu et al. (2013) and Gypser et al. (2018). However, no trend is observed between SSA and Al content by Namayandeh and Kabengi (2019). The ferrihydrites have the highest SSA of the studied (oxy)hydroxides, which are about 100, 50, and 10 times higher than the SSA of AlO(OH), GaO(OH), and the goethite series, respectively.

The PDF measurements of the ferrihydrite series (Fig. 3) show variations in oscillation amplitude as a function of substitution, with the Ga substituted ferrihydrites having a greater amplitude and the Al substituted ferrihydrites a smaller amplitude than the pure phase. This is the result of atomic mass differences: the heavier the atom, the greater the amplitude of the signal.

In addition, the amplitude of the oscillations decreases with increasing r and the oscillations completely disappear at $r > 22.5$ Å for the pure and Ga substituted ferrihydrite. This attenuation of amplitude indicates a lack of coherency at greater distances that is common for

Table 4
TG/DTA results of the ferrihydrite series, showing the initial weight, temperature of the dehydration and dehydroxylation peaks, weight lost after dehydration and dehydroxylation, and the calculated weight percentage (wt%) of H2O and OH. As there was no clear plateau between the dehydration and dehydroxylation reactions in the thermogravimetric data, the weight lost at 300 °C was chosen as this temperature lies halfway between the two peaks. OH loss was calculated as the difference between the value at 300 °C and the final plateau.

	Initial weight (mg)	T H_2O peak	mg lost H_2O	Wt% H_2O	T OH peak	mg lost OH	Wt% OH
Fh	65.9	117.4	16.2	25	378.2*	1.7	3.5
Fh20Al	67.9	119.3	18.9	28	361.6	3.0	6.0
Fh35Al	68.5	131.3	16.6	24	318.1	5.2	10
Fh10Ga	66.8	117.3	16.8	25	357.1	1.7	3.5
Fh20Ga	68.1	124.5	13.9	20	361.4	1.7	3.0
AlO (OH)	65.9	131.4	21.8	33	325.0	11.9	27

* value for the exothermal peak occurring at the same temperature as the dehydroxylation.

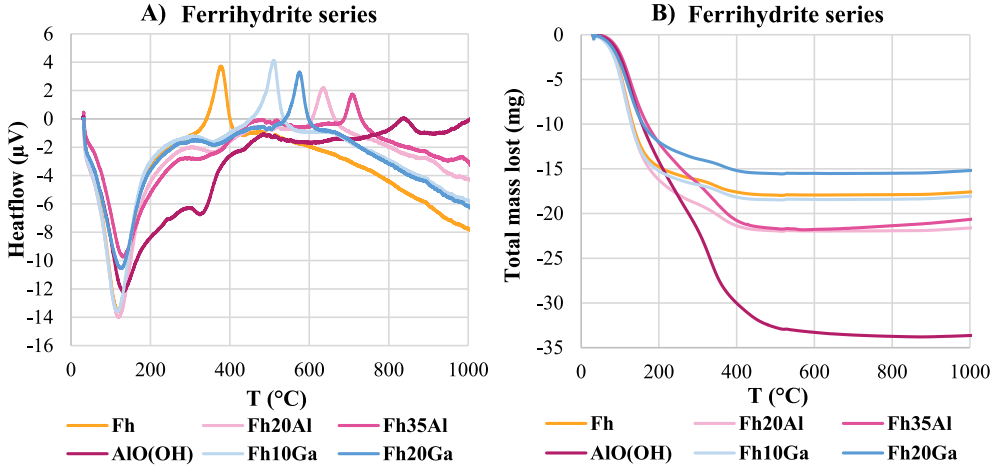

Fig. 2. A) Differential Thermal Analysis (DTA) and B) Thermogravimetric Analysis (TGA) of the ferrihydrite series.

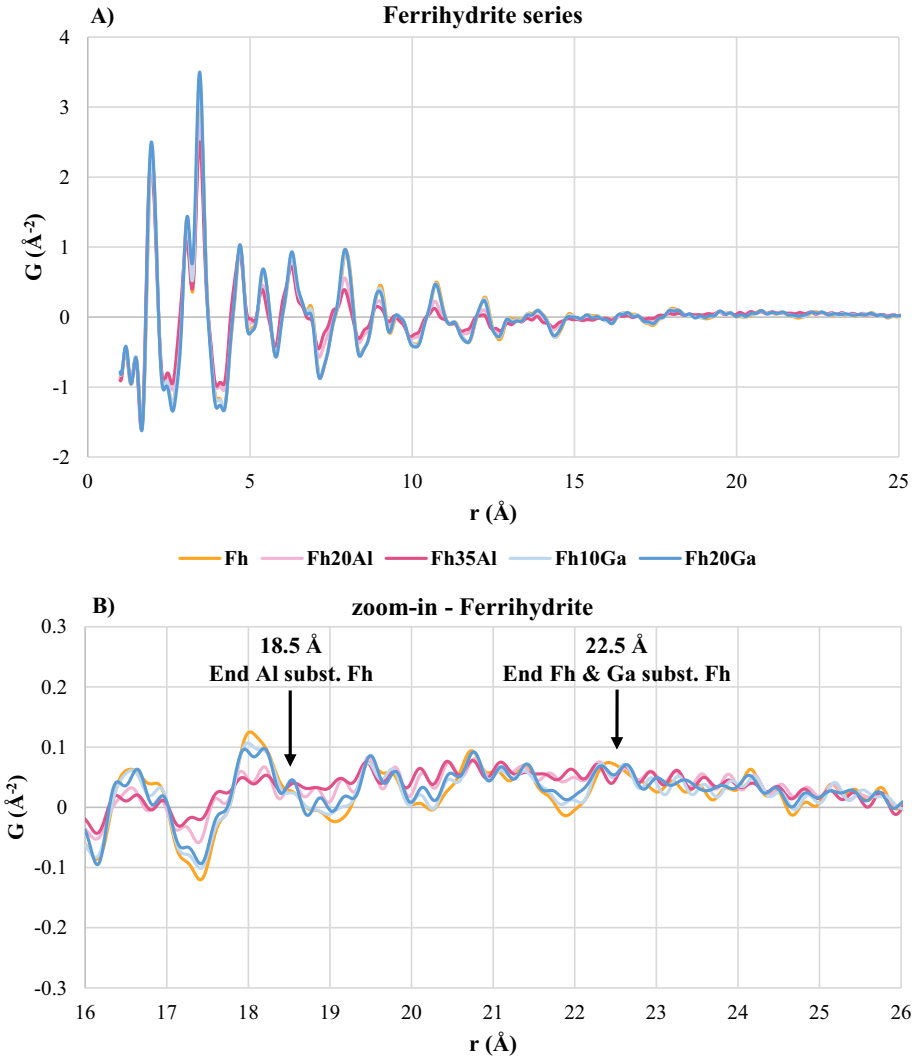

Fig. 3. PDF result of A) the ferrihydrite series, with B) showing a zoomed in section of the ferrihydrite series to show the distance at which the large overall oscillation, and thus the coherent domain, disappears.

amorphous material (Bordet, 2015), and a domain of coherency of 22.5 Å was previously found for 2d ferrihydrite by Michel et al. (2007). Contrary to the Ga, Al substitution reduces the domain size to 18.5 Å.

Inconsistencies between SSA evolution (Table 3) and particle size (Fig. 3) can be pointed out for the poorly crystalline series and the AlO(OH). Fh35Al, which has smaller particle size, should have a larger SSA than pure Fh. Thereby, according to the TEM images (Fig. S8), AlO(OH) having the smallest SSA is questionable. Several studies have indicated that the drying of poorly crystalline (oxy)hydroxides for N_2 adsorption and BET analysis causes the aggregation of the (oxy)hydroxides, resulting in an underestimation of the true SSA values (Hiemstra et al., 2019; Johnston et al., 2002; Villalobos and Antelo, 2011). In the ferrihydrite series, presuming a density of 3.5 g cm^{-3} and a spherical shape (Hiemstra, 2013), the SSA values correspond to particle diameters ranging from 5.05 (Fh and Fh10Ga) to 8.65 nm (Fh35Al). However, supposing that AlO(OH) and Fh have a similar density, this would mean that the AlO(OH) particles should have a diameter of 650 nm, which is much larger than what is observed in the TEM images (Fig. S8). Furthermore, these particle sizes inferred from the SSA are inconsistent with the domains of coherency found through PDF measurements (Fig. 3). The pure and Ga substituted ferrihydrites have a domain of coherency of 2.25 nm, which is less than half the particle size calculated from the SSA. Meanwhile, Al substitution decreases the domain of coherency, and thus the particle size, to 1.85 nm. This particle size is far smaller than the one calculated using the SSA, and the decrease in size with increasing Al content is the opposite of the trend seen with the SSA. However, the PDF results concur with previous studies of both pure and substituted Fh (Cismasu et al., 2014; Michel et al., 2007; Hiemstra, 2013, and the PDF particle size is more conform the TEM images (Fig. S8).

This decrease in particle size as a function of increasing Al content can also be observed in the TGA results (Fig. 2, Table 4). Hiemstra (2013) has shown that the water content of nanoparticles is inversely related to particle size, with smaller particles containing more water. Therefore, the increase in OH content (from 3 to 10 wt%) in the Al substituted Fh indicates that the particle size decreases with substitution. Based on the calculations in Hiemstra (2013), the AlO(OH) particles (27 wt% OH) should be half the size of the Fh35Al particles.

3.4. Phase and substitution dependency of the pH adsorption edge and the amount of REE adsorbed

For all (oxy)hydroxides the sum of elements adsorbed is phase and pH dependent (Fig. 4). The Fh is the only pure (oxy)hydroxide that reaches total adsorption, which occurs around pH 6.5, and adsorption capacity decreases along the trend of Fh > AlO(OH) ≅ Goe > GaO(OH) (Fig. 4A). A similar shift of the pH edge to around 0.5 pH point higher from Fh to Goe has previously been observed when studying radium and

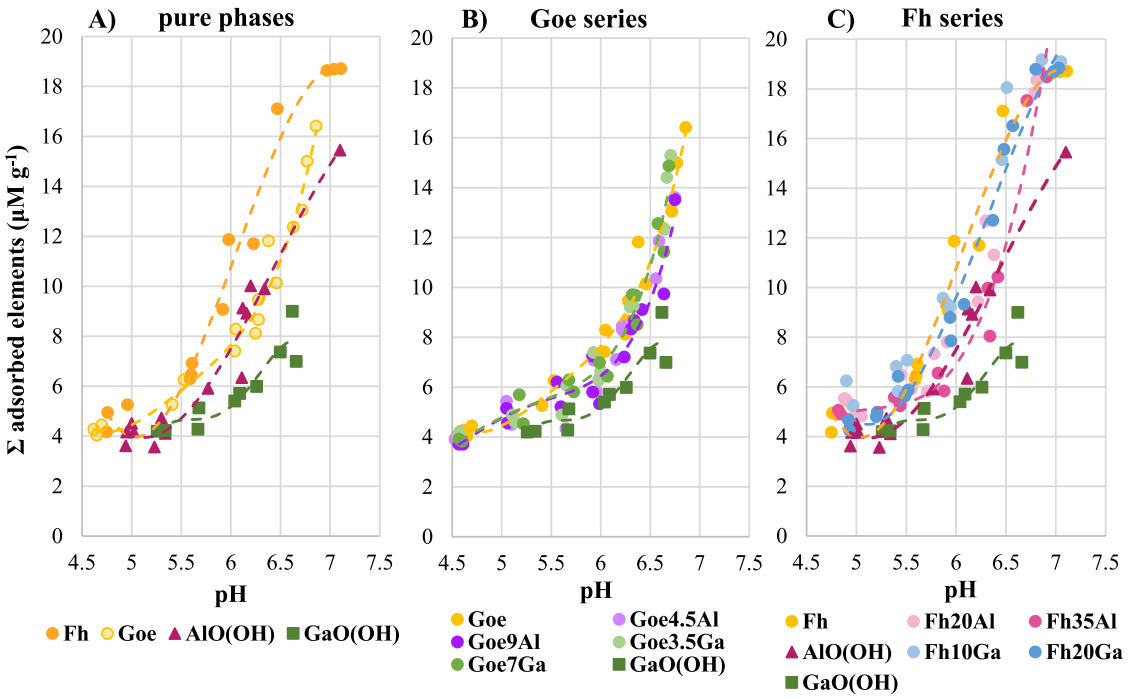

Fig. 4. Sum all elements adsorbed in µM g^{-1} compared to pH for A) the pure phases, B) the Goe series and GaO(OH), and C) the Fh series, AlO(OH), and GaO(OH).

uranium adsorption (Sajih et al., 2014; Wang et al., 2021).

The substitution in the goethite has little to no effect on total adsorption, with only the Goe9Al shifting to slightly higher pH (Fig. 4B). In the ferrihydrite on the other hand, there is a shift to higher pH of up to 0.5 pH point as a result of substitution. This shift to higher pH increases with an increase in substitution and is greater for the Al than the Ga, resulting in the following trend Fh ≅ Fh10Ga < Fh20Ga < Fh20Al < Fh35Al < AlO(OH) (Fig. 4C). In spite of the shift to higher pH, all ferrihydrites adsorb nearly 100% of the elements in solution at pH 7.

The variations in the amount of elements adsorbed and in the slope of the pH adsorption edge, are linked to the amount of complexation sites available at the surface of the different phases as a function of pH. This is predominantly linked to the size and SSA of the particles for a given mass. In the goethite series the low substitution rate (<10%) has little to no effect on the adsorption capacity, the SSA and size of the substituted goethites. On the other hand, the GaO(OH) has a lower SSA, is larger, and has a lower adsorption capacity than the substituted goethites (Table 3, Fig. S7, Fig. 4).

When taking the ferrihydrites into consideration, the previous section has shown that the size of the particles is a more reliable component than the SSA as the latter is often underestimated. However, the decrease from Fh > AlO(OH) ≅ Goe > GaO(OH) in both total adsorption and pH edge position cannot be directly linked to the particle size. Indeed, although the Fh size is smaller than that of Goe, which in turn is smaller than GaO(OH), the AlO(OH) particles should be smaller than the Fh particles, based on their OH content (Table 4), and thus adsorb more. The same is true for the trend in pH adsorption edge positions of the ferrihydrite series: Fh ≅ Fh10Ga < Fh20Ga < Fh20Al < Fh35 Al < AlO (OH), which cannot be explained by the variation in particle size AlO (OH) < Fh35 Al < Fh20Ga ≅ Fh nor by the variation in their pH_{PZC} (Fh < Fh10Ga ≅ Fh20Al < Fh20Ga < Fh35Al < AlO(OH)).

Since the substitution, with both Al and Ga, reduces the ferrihydrite adsorption capacity with a trend that cannot be explained by size or by pH_{PZC} variations, there must be another factor impacting the adsorption capacity. As no steps were taken to dissociate the poorly crystalline (oxy)hydroxides during the adsorption experiments, the aggregates could remain partially intact in solution. This could explain the shift in pH edge. Another explanation could be that substitution, by both Al and Ga, leads to a decrease in adsorption site density.

3.5. Adsorption complexes formed by REE

The Nd L_3-edge EXAFS spectra of Nd adsorbed on all (oxy)hydroxides are reported in Fig. 5A, along with the fit results. The corresponding Fourier transform (FT) and the fits are reported in Fig. 5B. The EXAFS spectra show monotonous oscillations with a maximum amplitude at 5.2 $Å^{-1}$ and a shoulder, whose visibility varies across the (oxy)hydroxides, at 6.5 $Å^{-1}$. The corresponding FT show that, for all (oxy)hydroxides, a high intensity first neighbour shell peak occurs at 2.0 Å. It is followed by a less intense second shell neighbour massif in the range of 2.8–3.8 Å, and a third neighbour shell from 3.8 to 4.6 Å. The first peak of the FT can be fitted with O neighbours, whose distances can be split between 2.43 and 2.48 Å and 2.59–2.63 Å (Table 5). The second neighbour massif can be fitted with Me (i.e. Fe, Al, or Ga) neighbours at two distances, 3.04–3.42 Å and 3.51–3.72 Å, except for the AlO(OH), whose EXAFS signal can be fitted with a single Nd—Al distance at 3.51 Å (Table 5). These distances found through fitting are in agreement with literature (Nakada et al., 2013; Ohta et al., 2009). The smallest Nd-Me1 distance can be assigned to the formation of bidentate mononuclear (BM) complexes, where the Nd is bound to two O of one single metal octahedra. The second Nd-Me2 distance can be assigned to the formation of bidentate binuclear (BB) complexes, where the Nd is bound to two O belonging to two adjacent metal octahedra bound to one another along their edge. The existence of both complexes at the surface of ferrihydrite and goethite has already been demonstrated (Ona-Nguema et al., 2005; Qin et al., 2021). The third shell of neighbours can be fitted with O belonging to the structure of the adsorbing (oxy)hydroxide, at 4.24–4.33 Å and 4.53–4.60 Å.

The EXAFS fit gives the relative amount of BM and BB complexes formed by Nd on the different (oxy)hydroxides (BM% is N_Fe1 in %, and BB% is half N_Fe2 in % in Table 5). The 200-Goe, with the lowest amount of Nd adsorbed, has the highest amount of BM complexes in percentage (70%). For the experiments performed with 1000 µgL^{-1}, the BM complexes represent between 10 and 30% of all complexes, with the exception of AlO(OH) which shows no BM sites (Fig. 6). This result is in agreement with the literature, where it is shown that various Al (oxy)

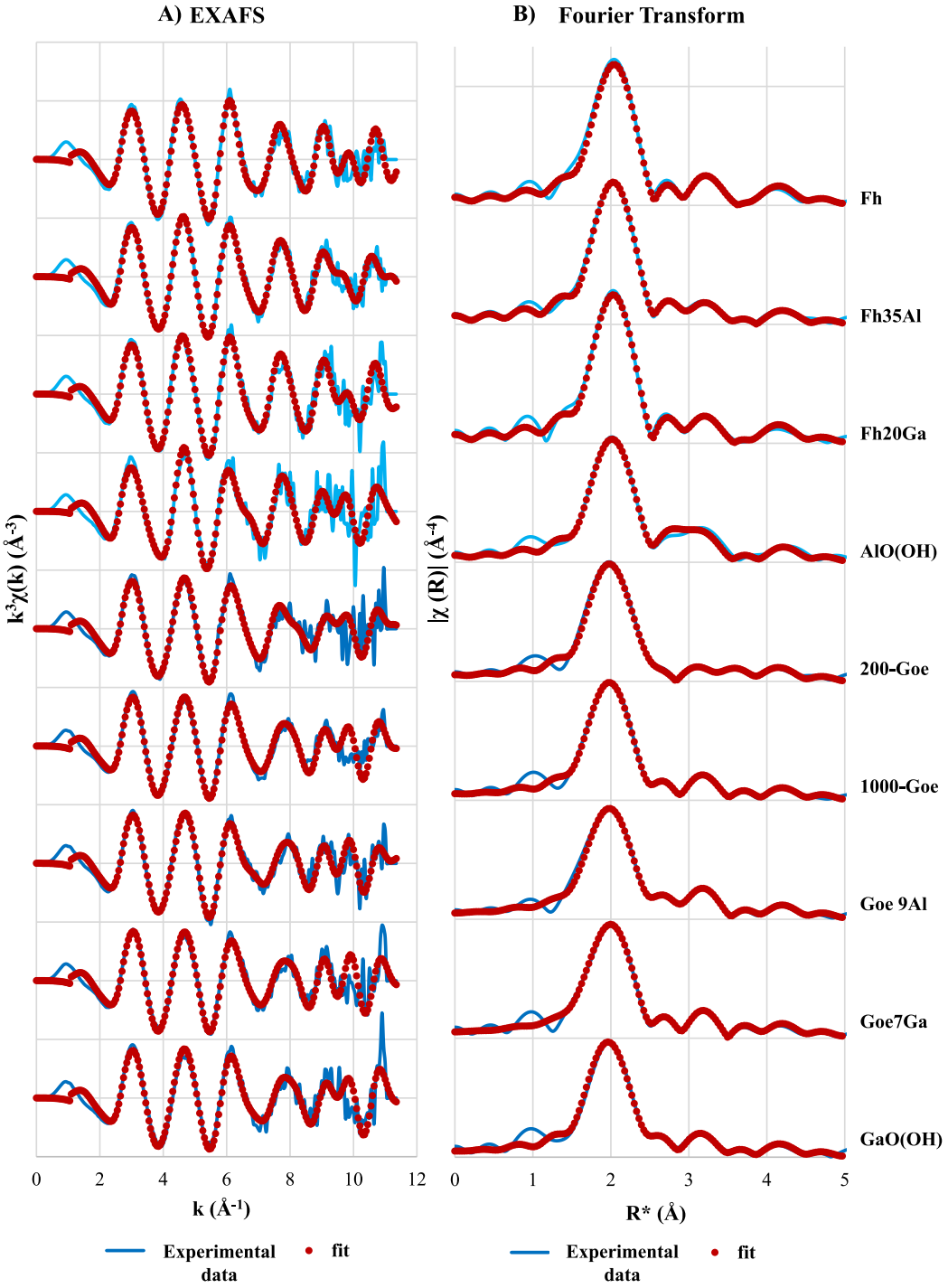

Fig. 5. Nd L_3-edge A) EXAFS, and B) Fourier Transform, with R* distances not corrected from phase shift, for Nd adsorbed on all metal oxyhydroxides. Adsorption was performed with [Nd] = 1000 μg L^{-1}, with the exception of 200 -Goe for which [Nd] = 200 μg L^{-1}. The solid blue line is for the experimental data and the dotted red line represents the fit, and the name of the (oxy)hydroxides are displayed on the right with the sequence being the same for both A) and B). (For interpretation of the references to colour in this figure legend, the reader is referred to the web version of this article.)

hydroxides exclusively sorb as BB complexes (Kappen and Webb, 2013; Xu and Catalano, 2016).

3.6. Impact of substitution on adsorption site availability

3.6.1. Number of adsorption complexes on goethite

The speciation of adsorbed Nd has shown that REE can form two types of complexes, BM and BB, in varying proportions (Figs. 5 and 6, Table S17). In goethite the BM complexation sites, located on the (021) plane at the 'tip' of the needle, have a higher affinity for metals than the more abundant sites on which BB complexes form, located on the (110) plane on the side of the needle (Fig. S9) (Sherman et al., 2008; Qin et al., 2021). Thus, the BM complexes dominate adsorption at the start, and once they are saturated, the adsorption shifts to BB complexation sites.

Table 5
Nd EXAFS fit results. N is the amount of neighbours, σ^2 the Debye-Waller factor and R the distance in Å. R-factor is a factor of fit quality, the measure of the percentage misfit between the data and theory. $S_0^2 = 1.09$, $\Delta E = 4.5$ eV based on the Nd_2O_3 reference fit (Fig. S6, Table S16). Constraints applied to the fit parameters are: On the first shell, N_O1 + N_O2 = 8 (Duvail et al., 2008; Ohta et al., 2009), σ^2_O1 and σ^2_O2 were set to 0.004. REE was expected to sorb on either one edge of a singular octahedra and have 1 metal neighbour through bidentate mononuclear (BM) binding, or on corners of two adjacent octahedra and have 2 metal neighbours through bidentate binuclear (BB) binding (Sherman et al., 2008; Hiemstra and Van Riemsdijk, 2009; Qin et al., 2021). Then the sum of neighbours from the two metal (Me, i.e. Fe, Al or Ga) distances was set to N_Me1 + (0.5*N_Me2) = 1. N_O3 + N_O4 = 8, based on the amount of oxygen neighbouring, at this distance, elements adsorbed on either in BM or BB binding modes. The Deby Waller factors were set to 0.005.

Oxyhydr.	N_O1 N_O2	R_O1 R_O2	σ^2_O1	N_Fe1	R_Fe1	σ^2_Fe1	N_Fe2	R_Fe2	σ^2_Fe2	N_O3	R_O3	σ^2_O3	N_O4	R_O4	σ^2_O4	R-factor
1000-Goe	4.9 ± 0.04 3.1*	2.45 ± 0.001 2.61 ± 0.002	0.004* 0.004*	0.2 ± 0.07	3.38 ± 0.02	0.002 ± 0.001	1.6*	3.63 ± 0.02	0.007*	4.2 ± 0.29	4.25 ± 0.01	0.005*	3.8* ±	4.55 ± 0.01	0.005*	0.0039
200-Goe	5.0 ± 0.04 3.0*	2.45 ± 0.001 2.62 ± 0.002	0.004* 0.004*	0.7 ± 0.07	3.08 ± 0.02	0.013 ± 0.003	0.6*	3.67 ± 0.01	0.007*	4.0 ± 0.29	4.26 ± 0.01	0.005*	4.0*	4.55 ± 0.01	0.005*	0.0073
Goe9Al	4.5 ± 0.06 3.5*	2.43 ± 0.002 2.60 ± 0.002	0.004* 0.004*	0.4 ± 0.07	3.24 ± 0.02	0.013 ± 0.003	1.2*	3.64 ± 0.01	0.004*	4.4 ± 0.37	4.25 ± 0.01	0.005*	3.6*	4.55 ± 0.02	0.005*	0.0086
Goe7Ga	4.4 ± 0.07 3.6*	2.43 ± 0.002 2.59 ± 0.003	0.004* 0.004*	0.3 ± 0.04	3.34 ± 0.02	0.002 ± 0.001	1.4*	3.61 ± 0.01	0.005*	4.6 ± 0.35	4.24 ± 0.01	0.005*	3.4*	4.54 ± 0.02	0.005*	0.0049
	N_O1 N_O2	**R_O1 R_O2**	**σ^2_O1**	**N_Ga1**	**R_Ga1**	**σ^2_Ga1**	**N_Ga2**	**R_Ga2**	**σ^2_Ga2**	**N_O3**	**R_O3**	**σ^2_O3**	**N_O4**	**R_O4**	**σ^2_O4**	**R-factor**
GaO(OH)	5.1 ± 0.06 2.9*	2.45 ± 0.001 2.63 ± 0.005	0.004* 0.004*	0.3 ± 0.04	3.04 ± 0.01	0.009 ± 0.003	1.4*	3.61 ± 0.01	0.007*	4.1 ± 0.31	4.24 ± 0.01	0.005*	3.9*	4.53 ± 0.01	0.005*	0.0050

Oxyhydr.	N_O1 N_O2	R_O1 R_O2	σ^2_O1	N_Fe1	R_Fe1	σ^2_Fe1	N_Fe2	R_Fe2	σ^2_Fe2	N_O3	R_O3	σ^2_O3	N_O4	R_O4	σ^2_O4	R-factor
Fh	4.4 ± 0.17 3.6*	2.46 ± 0.003 2.59 ± 0.004	0.004* 0.004*	0.3 ± 0.10	3.42 ± 0.02	0.002 ± 0.001	1.4*	3.64 ± 0.01	0.004*	3.3 ± 0.79	4.24 ± 0.03	0.005*	4.7*	4.57 ± 0.02	0.005*	0.0093
Fh35Al	5.2 ± 0.09 2.8*	2.48 ± 0.001 2.61 ± 0.003	0.004* 0.004*	0.1 ± 0.12	3.26 ± 0.05	0.006*	1. 8*	3.72 ± 0.01	0.012 ± 0.001*	3.4 ± 0.51	4.33 ± 0.01	0.005*	4.6*	4.60 ± 0.01	0.005*	0.0033
Fh20Ga	5.3 ± 0.15 2.7*	2.48 ± 0.002 2.61 ± 0.005	0.004* 0.004*	0.2 ± 0.12	3.37 ± 0.04	0.006 ± 0.002	1.2*	3.66 ± 0.01	0.007*	3.2 ± 0.77	4.26 ± 0.02	0.005*	4.8*	4.57 ± 0.02	0.005*	0.0074
	N_O1 N_O2	**R_O1 R_O2**	**σ^2_O1**	**N_Al1**	**R_Al1**	**σ^2_Al1**	**N_Al2**	**R_Al2**	**σ^2_Al2**	**N_O3**	**R_O3**	**σ^2_O3**	**N_O4**	**R_O4**	**σ^2_O4**	**R-factor**
AlO(OH)	5.2 ± 0.13 2.8*	2.47 ± 0.002 2.63 ± 0.004	0.004* 0.004*				2.0*	3.54 ± 0.01	0.003 ± 0.001	3.1 ± 0.70	4.32 ± 0.02	0.005*	4.9*	4.59 ± 0.01	0.005*	0.0075

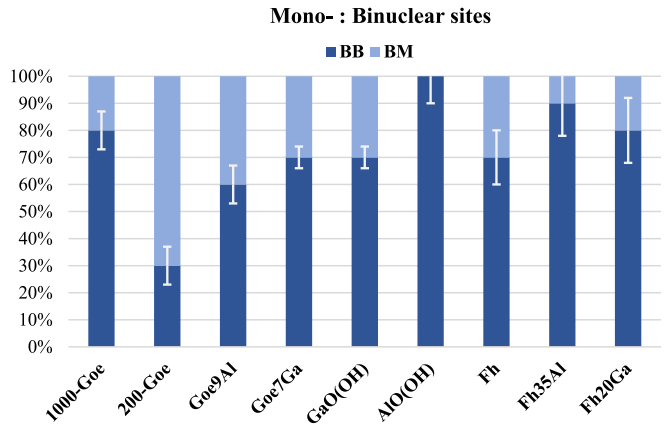

Fig. 6. Ratio of mononuclear (BM) to binuclear (BB) sites occupied by Nd, with the error bars related to the standard deviation of the number of metal neighbour parameter given by ARTEMIS.

This is confirmed by the EXAFS fits, which show that the ratio between BM and BB complexation sites shifts from 70:30 to 20:80 from the 200Goe to the 1000Goe (Fig. 6).

Knowing the amount of Nd adsorbed, the SSA of the goethites, and the percentage of BM complexes formed, it is possible to calculate the amount of maximum available BM complexing sites per surface unit for each goethite. When plotting it against the SSA, a clear quadratic polynomial relationship can be observed, allowing the extrapolation of the non-measured goethite (Fig. 7). The amount of BM complexes increases with decreasing SSA, thus increasing size. These results are in agreement with the TEM observations (Fig. S7). With the increase in particle size of the goethite from the Fe to the Ga end member, the proportion of the (021) plane at the tip of the needle increases.

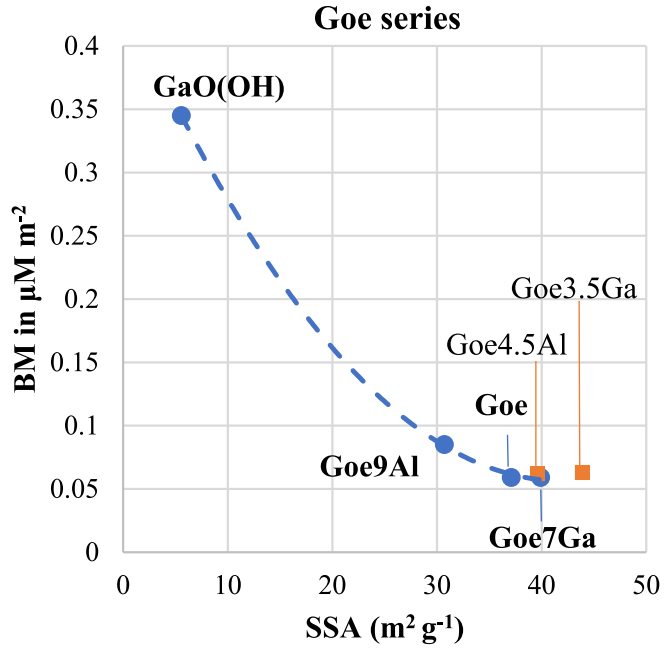

Fig. 7. Bidentate mononuclear (BM) sites vs. specific surface area (SSA) of the crystalline oxyhydroxides. The blue dots were calculated from the EXAFS fit data and fitted with a trendline. This trendline is described by $y = 2.23*10\text{-}4x^2 – 1.83*10\text{-}2x + 0.44$. From the trendline equation the orange squares were calculated for the intermediate substitutions (no EXAFS recorded on these samples). (For interpretation of the references to colour in this figure legend, the reader is referred to the web version of this article.)

3.6.2. *Impact of substitution on shape and site availability of ferrihydrite*

Since we have demonstrated that the SSA of the ferrihydrite series is not a reliable metric, the relationship between the amount of BM complexes that can form and the substitution rate in the ferrihydrites will be assessed per mass of (oxy)hydroxide. Using the results from the pH adsorption edge to calculate the total amount of elements adsorbed at pH 6.5, during the pH edge adsorption experiments, the relationship between the loss in total adsorption and the loss in BM complexes with substitution is illustrated in Fig. 8A. In this figure the loss in total adsorption between the Fh and the Fh20Ga falls along the 1:1 trend, indicating that the loss in total adsorption is directly related to the decrease in BM complexes formed at the surface.

Hiemstra (2013) described three possible idealized shapes for Fh (sphere, oblong sphere, and hexagonal cylinder), all of which are described by non-reactive (001) and (00−1) planes at the top and bottom of the particle and reactive surface described by the (1–10) and (1–1-1) planes (Fig. 9). With the most plausible shape being the "spherical" one. The reactive planes contain layers with alternating terminations allowing for either BM or BB complex formation (Fig. 9B and C). On the (1–1-1) plane the ratio of BM:BB cannot be modified, however on the (1–10) plane the BB:BM ratio depends on the crystal termination of the layer on which BM complexes can form (Fig. 9C). When the protrusions of iron octahedra are missing, the adsorption sites allowing for BM complexation are unavailable. Consequently, the decrease in BM complexes between Fh and Fh20Ga, while maintaining the particle size and spherical shape, can be explained by the Ga substitution affecting the crystal termination of the layer containing the BM complexation sites on the (1–10) plane, limiting the protrusion of iron octahedra, and thus reducing adsorption site density. The rise in pH_{PZC} with Ga substitution could then be a consequence of the decrease in BM complexation sites, as the BM complexes form at lower pH than the BB complexes.

The Fh35Al and AlO(OH) do not fall along the 1:1 line of decreasing adsorption and decreasing BM complexes, nor do they fall along the same trend line of decrease in total adsorption with increasing pH_{PZC} (Fig. 8).

From the Nd EXAFS data fit (Table), and from literature (Kappen and Webb, 2013; Xu and Catalano, 2016), it is known that the AlO(OH) does not form any BM adsorption complexes. This can only occur if there are no (1-1-1) surface planes present at the AlO(OH) surface, as BM complexation sites cannot be removed from these planes (Hiemstra, 2013). Thus we can hypothesize that the decrease in pH_{PZC} of the Al substituted ferrihydrites and the AlO(OH), compared to the pure and Ga substituted ones, is due to the loss of the (1–1-1) surface planes (Fig. 9B). This would mean the AlO(OH), Fh20Al, and the Fh35Al particles have a hexagonal cylinder shape, smaller than the sphere proposed for the pure and Ga substituted ferrihydrite (Hiemstra, 2013). The decrease in adsorption capacity seen with Al substitution is enhanced by this difference in shape, as the number of reactive sites is higher on the spherical compared to the cylindrical particles, 85% and 67% respectively (Hiemstra, 2013). As there is little difference in the pH_{PZC} between the (1-10) and (1-1-1) surface planes (Hiemstra, 2013), the loss of the (1-1-1) planes between Fh20Ga and Fh20Al does not modify the overall pH_{PZC} of the ferrihydrite even though it dramatically alters their adsorption capacity. The trendline describing the decrease in adsorption with increasing pH_{PZC} of the Al substituted Fh and AlO(OH) runs parallel to the one of the pure and Ga substituted Fh (Fig. 8B), revealing that the decrease in total adsorption from Fh20Al to AlO(OH) is also only the result of a reduction in BM complexation sites through changes in crystal terminations on the (1–10) plane. Then, as for the Ga substitution, the pH_{PZC} increases with a decrease in BM complexes because these complexes form at lower pH.

In conclusion, both Ga and Al substitution reduce the amount of BM complexation sites available at the ferrihydrite surface, however Al substitution also inhibits the formation of the (1-1-1) plane.

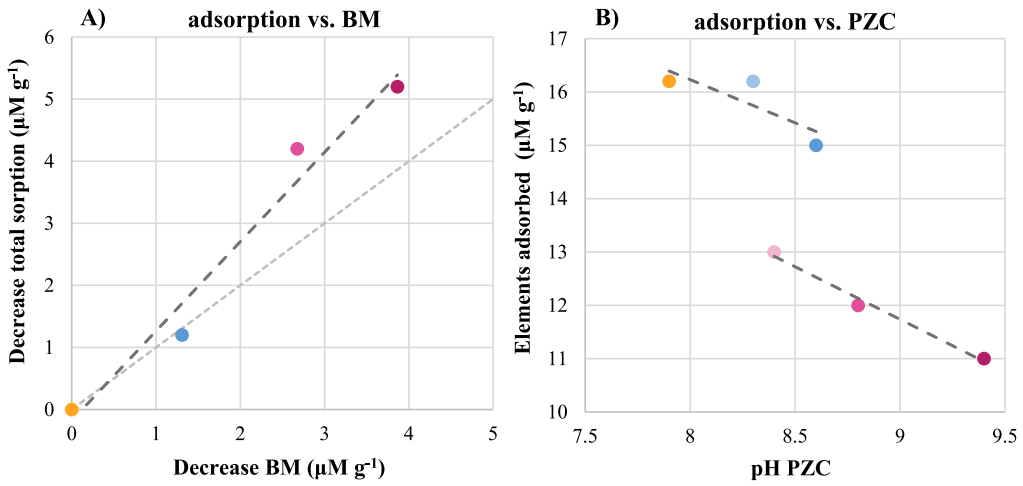

Fig. 8. Using the pH edge adsorption data to plot A) the difference in adsorption between Fh and Fh20Ga, Fh35Al, and AlO(OH) at pH 6.5 compared to the amount of BM sites per gram for each phase. With the dark grey line denoting the trend between the data points and the light grey line denoting the 1:1 line. And to plot B) total adsorption of the poorly crystalline phases at pH 6.5 against pH_{PZC}. In both graphs the orange dot represents the pure Fh, the light and dark blue represent the Fh10Ga and Fh20Ga, respectively, and the light, middle, and dark pink represent the Fh20Al, Fh35Al, and AlO(OH), respectively. (For interpretation of the references to colour in this figure legend, the reader is referred to the web version of this article.)

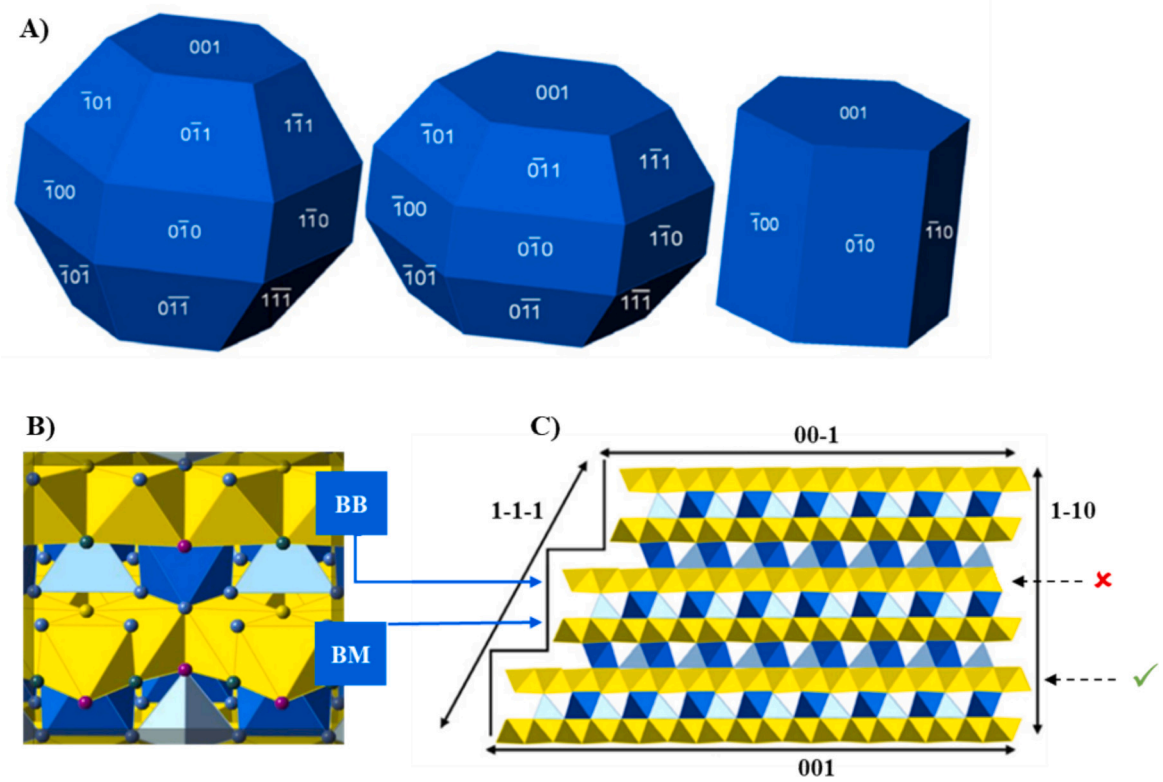

Fig. 9. Idealized ferrihydrite shape figure adjusted from Fig. 7 in Hiemstra et al., 2013. A) idealized Fh shapes and their respective surfaces, B) sorption site morphology, and C) crystal terminations as found on each type of plane. With the difference in BM complex sorption site variation on the (1–10) plane indicated by the dashed arrows, the tick mark indicating an available sorption site and the cross an unavailable adsorption site.

4. Conclusion

REE adsorption experiments have been carried out at acidic to near neutral pH, on a series of goethites and ferrihydrites substituted with Al or Ga. In addition, REE complexation modes were studied by EXAFS collected at the Nd L_3-edge. These experiments have shown that REE adsorption increases with increasing pH, due to the concomitant increase in deprotonation of the surface sorbing sites. At a given pH, the size of the mineral phase and the adsorption site distribution and density are the factors controlling the quantity of REE adsorbed. The substitutions in goethite are too low to have a significant impact on the amount of elements adsorbed. On the contrary, adsorption on ferrihydrite decreases with the increasing substitution rate, as the substitution leads to a decrease in particle shape, size and adsorption site density.

Two types of adsorption sites were shown to exist at the surface of the studied (oxy)hydroxides, which allow the formation of either BM or BB complexes. The decrease in adsorption site density with increasing substitution of Al and Ga in ferrihydrite is linked to a decrease in the

number of BM complexation sites, through inhibition of the formation of iron octahedra protrusions at the (1–10) surface planes. In addition, when it comes to the Al substituted ferrihydrites, a change in particle shape occurs from the spherical of the pure and Ga substituted Fh to the cylindrical shape also found for AlO(OH). This change in shape leads to the loss of the (1–1-1) surface planes, and thus the loss of adsorption sites for both BB and BM complexes.

By highlighting the essential role of substitution on the adsorption capacity of ferrihydrite, we offer new perspectives for understanding the behaviour of REE in environmental systems. In natural surface and groundwaters, ferrihydrite colloids play a key role in trapping metallic pollutants, including REE. In this work we have shown that, while adsorption increases with pH, it is also strongly influenced by structural modifications in the adsorbent phase related to substitutions which modify adsorption site density and distribution. Thus, substitutions of Fe by Al, which is widely available in natural environments, will have a direct impact on the role of ferrihydrite in trapping REE:

1/ The mobility of REE will be enhanced as the size of the Al-substituted Fh is smaller. Thus, these particles will have more ability to remain in suspensions or to be transported in soil or sediment porosity. Furthermore, the reduction in adsorption site density caused by Al-substitution will reduce the quantity of REE adsorbed, which means more REE will remain in solution where they will then be more mobile.

2/ The bioavailability of REE will be enhanced as the amount of REE adsorbed by Al-substituted Fh is reduced. A greater quantity of REE in solution will then be potentially taken up by plants or aquatic organisms, presenting a higher risk of toxic effects (Forsyth et al., 2023; Lachaux et al., 2022; Le Jean et al., 2023; Revel et al., 2023).

3/ The formed "REE - Al-substituted Fh" complexes will be more stable over time as Al-substitution have been demonstrated to preserve Fh from aging phase transformation (Schwertmann et al., 2000) and either abiotic or biotic reductive dissolution (Masue-Slowey et al., 2011).

CRediT authorship contribution statement

Anne Buist: Writing – original draft, Visualization, Project administration, Methodology, Investigation, Formal analysis, Conceptualization. **Camille Rivard:** Writing – review & editing, Supervision, Conceptualization. **Mélanie Davranche:** Writing – review & editing, Supervision, Methodology, Funding acquisition. **Francois Brisset:** Writing – review & editing, Investigation. **Khalil Hanna:** Writing – review & editing, Investigation. **Erwan Paineau:** Writing – review & editing, Data curation. **Stéphan Rouzière:** Writing – review & editing, Investigation, Data curation. **Erik Elkaim:** Writing – review & editing, Investigation, Data curation. **Stéphanie Blanchandin:** Writing – review & editing, Resources. **Karine Chaouchi:** Writing – review & editing, Investigation. **Claire Hotton:** Investigation. **Aline Dia:** Writing – review & editing, Funding acquisition. **Delphine Vantelon:** Writing – review & editing, Supervision, Project administration, Methodology, Formal analysis, Conceptualization.

Declaration of competing interest

The authors declare that they have no known competing financial interests or personal relationships that could have appeared to influence the work reported in this paper.

Data availability

The main data is in the supplementary information, and the raw XRD and TG/DTA data has been published using Mendeley data and can be found using the DOI provided at the end of the article.

Acknowledgements

This article is part of the ITN PANORAMA project. It has received funding from European Union's Horizon 2020 research and innovation program under the Marie Sklodowska-Curie Grant Agreement N°857,989.

We acknowledge the SOLEIL synchrotron for allocating beamtime on the CRISTAL (BAG proposal 20,211,378, in the framework of the CNRS RECIPROCS network) and the LUCIA (proposals 20,210,638 & 20,220,932) beamlines. We warmly thank both the CRISTAL and LUCIA teams for their support during the experiments and for the data analysis.

Appendix A. Supplementary data

Tables S1-3 contain the major elements, trace elements, and REE present in the synthetic Fe/Al/Ga (oxy)hydroxides. Tables S4–15 contain the parameters and results of the pH adsorption edge experiments for each (oxy)hydroxide, used to calculate the amount of REE adsorbed for Fig. 3. Table S16 contains the EXAFS fit results of the Nd_2O_3 reference, and Table S17 gives an overview of the results of the Nd adsorption experiment.

Figs. S1–5 contain the whole profile pattern matching of the goethite XRD data. Fig. S6 shows the EXAFS and Fourier Transform of the Nd_2O_3 reference at the L3-edge. Fig. S7 and S8 contain the TEM images of the (oxy)hydroxides, and Fig. S9 shows the shape, structure, and the different binding sites on Goe.

The datasets for the XRD and TG/DTA measurements are available on Mendeley Data under DOI: 10.17632/c7bgzd2z4g.1

References

Adra, A., Morin, G., Ona-Nguema, G., Brest, J., 2016. Arsenate and arsenite adsorption onto Al-containing ferrihydrites. Implications for arsenic immobilization after neutralization of acid mine drainage. Appl. Geochem. 64, 2–9.

Bau, M., 1999. Scavenging of dissolved yttrium and rare earths by precipitating iron oxyhydroxide: experimental evidence for Ce oxidation, Y-Ho fractionation, and lanthanide tetrad effect. Geochim. Cosmochim. Acta 63 (1), 67–77.

Bau, M., Dulski, P., 1996. Anthropogenic origin of positive gadolinium anomalies in river waters. Earth Planet. Sc. Lett. 143 (1–4), 245–255.

Bookhagen, B., Bastian, D., Buchholz, P., Faulstich, M., Opper, C., Irrgeher, J., Koeberl, C., 2020. Metallic resources in smartphones. Res. Policy 68, 101750.

Bordet, P., 2015. Local structure studies using the pair distribution function. In: EPJ Web of Conferences, vol. 104. EDP Sciences, p. 01003.

Bradley, S.M., Kydd, R.A., Yamdagni, R., 1990. Comparison of the hydrolyses of gallium (III) and aluminium (III) solutions by nuclear magnetic resonance spectroscopy. J. Chem. Soc. Dalton Trans. 9, 2653–2656.

Brookins, D.G., 1983. Eh-pH diagrams for the rare earth elements at 25°C and one bar pressure. Geochem. J. 17, 223–229.

Brouziotis, A.A., Giarra, A., Libralato, G., Pagano, G., Guida, M., Trifuoggi, M., 2022. Toxicity of rare earth elements: an overview on human health impact. Front. Environ. Sci. 10, 948041.

Cánovas, C.R., Basallote, M.D., Macías, F., Olías, M., Pérez-López, R., Ayora, C., Nieto, J. M., 2021. Geochemical behaviour and transport of technology critical metals (TCMs) by the Tinto River (SW Spain) to the Atlantic Ocean. Sci. Total Environ. 764, 143796.

Carta, D., Casula, M.F., Corrias, A., Falqui, A., Navarra, G., Pinna, G., 2009. Structural and magnetic characterization of synthetic ferrihydrite nanoparticles. Mater. Chem. Phys. 113 (1), 349–355.

Castor, S.B., Hedrick, J.B., 2006. Rare earth elements. Industrial minerals and rocks 7, 769–792.

Cismasu, A.C., Michel, F.M., Stebbins, J.F., Levard, C., Brown Jr., G.E., 2012. Properties of impurity-bearing ferrihydrite I. Effects of Al content and precipitation rate on the structure of 2-line ferrihydrite. Geochim. Cosmochim. Acta 92, 275–291.

Cismasu, A.C., Levard, C., Michel, F.M., Brown Jr., G.E., 2013. Properties of impurity-bearing ferrihydrite II: Insights into the surface structure and composition of pure, Al-and Si-bearing ferrihydrite from Zn (II) sorption experiments and Zn K-edge X-ray absorption spectroscopy. Geochim. Cosmochim. Acta 119, 46–60.

Cismasu, A.C., Michel, F.M., Tcaciuc, A.P., Brown Jr., G.E., 2014. Properties of impurity-bearing ferrihydrite III. Effects of Si on the structure of 2-line ferrihydrite. Geochim. Cosmochim. Acta 133, 168–185.

Compton, J.S., White, R.A., Smith, M., 2003. Rare earth element behavior in soils and salt pan sediments of a semi-arid granitic terrain in the Western Cape, South Africa. Chem. Geol. 201 (3–4), 239–255.

Dai, S., Jiang, Y., Ward, C.R., Gu, L., Seredin, V.V., Liu, H., Ren, D., 2012. Mineralogical and geochemical compositions of the coal in the Guanbanwusu Mine, Inner Mongolia, China: further evidence for the existence of an Al (Ga and REE) ore deposit in the Jungar Coalfield. Int. J. Coal Geol. 98, 10–40.

Davranche, M., Pourret, O., Gruau, G., Dia, A., 2004. Impact of humate complexation on the adsorption of REE onto Fe oxyhydroxide. J. Colloid Interface Sci. 277 (2), 271–279.
De Oliveira, R.P., Benvenuti, J., Espinosa, D.C.R., 2021. A review of the current progress in recycling technologies for gallium and rare earth elements from light-emitting diodes. Renew. Sust. Energ. Rev. 145, 111090.
Dia, A., Gruau, G., Olivié-Lauquet, G., Riou, C., Molénat, J., Curmi, P., 2000. The distribution of rare earth elements in groundwaters: assessing the role of source-rock composition, redox changes and colloidal particles. Geochim. Cosmochim. Acta 64 (24), 4131–4151.
Duvail, M., Spezia, R., Vitorge, P., 2008. A dynamic model to explain hydration behaviour along the lanthanide series. ChemPhysChem 9 (5), 693–696.
Egler, S.G., Niemeyer, J.C., Correia, F.V., Saggioro, E.M., 2022. Effects of rare earth elements (REE) on terrestrial organisms: current status and future directions. Ecotoxicology 31 (5), 689–699.
Flank, A.M., Cauchon, G., Lagarde, P., Bac, S., Janousch, M., Wetter, R., Dubuisson, J.-M., Idir, M., Langlois, F., Moreno, T., Vantelon, D., 2006. LUCIA, a microfocus soft XAS beamline. Nucl. Instrum. Meth. B 246 (1), 269–274.
Forsyth, K., Dia, A., Marques, R., Prudencio, M.I., Diamantino, C., Carvalho, E., Russo, D., Dionisio, I., Davranche, M., Bouhnik-Le-Coz, M., Pedrot, M., 2023. Bioconcentration and translocation of rare earth elements in plants collected from three legacy mines sites in Portugal. Front. Environ. Sci. 11, 1191909 https://doi.org/10.3389/fenvs.2023.1191909.
Guimarães Jr., W.G., Ferreira de Lima, G., Duarte, H.A., 2023. Probing the Local Environment of Al-Substitution into Ferrihydrite using DFT+ U Calculations. J. Phys. Chem. C 127 (6), 3285–3294.
Gwenzi, W., Mangori, L., Danha, C., Chaukura, N., Dunjana, N., Sanganyado, E., 2018. Sources, behaviour, and environmental and human health risks of high-technology rare earth elements as emerging contaminants. Sci. Total Environ. 636, 299–313.
Gypser, S., Hirsch, F., Schleicher, A.M., Freese, D., 2018. Impact of crystalline and amorphous iron-and aluminum hydroxides on mechanisms of phosphate adsorption and desorption. J. Environ. Sci. 70, 175–189.
Haque, N., Hughes, A., Lim, S., Vernon, C., 2014. Rare earth elements: Overview of mining, mineralogy, uses, sustainability and environmental impact. Resources 3 (4), 614–635.
Hatje, V., Bruland, K.W., Flegal, A.R., 2016. Increases in anthropogenic gadolinium anomalies and rare earth element concentrations in San Francisco Bay over a 20 year record. Environ. Sci. Technol. 50 (8), 4159–4168.
Henderson, P., 1984. Rare Earth Element Geochemistry. Elsevier.
Hiemstra, T., 2013. Surface and mineral structure of ferrihydrite. Geochim. Cosmochim. Acta 105, 316–325.
Hiemstra, T., Van Riemsdijk, W.H., 2009. A surface structural model for ferrihydrite I: Sites related to primary charge, molar mass, and mass density. Geochim. Cosmochim. Acta 73 (15), 4423–4436.
Hiemstra, T., Mendez, J.C., Li, J., 2019. Evolution of the reactive surface area of ferrihydrite: time, pH, and temperature dependency of growth by Ostwald ripening. Env. Sci.: Nano 6 (3), 820–833.
Hissler, C., Montarges-Pelletier, E., Kanbar, H.J., Le Meur, M., Gauthier, C., 2023. Impact of past steel-making activities on lanthanides and Y (REY) fractionation and potential mobility in riverbank sediments. Front. Earth Sci. 10, 1056919.
Inoue, K., Fukushi, M., Furukawa, A., Sahoo, S.K., Veerasamy, N., Kurokawa, M., Hosokawa, S., 2020. Detection of anthropogenic gadolinium in river waters in Hokkaido, Japan. Jpn J. Educ. Radiol. Tech. 8, 11–16.
Itie, J.P., Baudelet, F., Briois, V., Elkaïm, E., Nadji, A., Thiaudière, D., 2012. Synchrotron radiation: instrumentation in condensed matter. X-Rays Mat. 1–47.
Jambor, J.L., Dutrizac, J.E., 1998. Occurrence and constitution of natural and synthetic ferrihydrite, a widespread iron oxyhydroxide. Chem. Rev. 98 (7), 2549–2586.
Johnston, C.T., Wang, S.L., Hem, S.L., 2002. Measuring the surface area of aluminum hydroxide adjuvant. J. Pharm. Sci. 91 (7), 1702–1706.
Kappen, P., Webb, J., 2013. An EXAFS study of arsenic bonding on amorphous aluminium hydroxide. Appl. Geochem. 31, 79–83.
Klaver, G., Verheul, M., Bakker, I., Petelet-Giraud, E., Négrel, P., 2014. Anthropogenic Rare Earth Element in rivers: Gadolinium and lanthanum. Partitioning between the dissolved and particulate phases in the Rhine River and spatial propagation through the Rhine-Meuse Delta (the Netherlands). Appl. Geochem. 47, 186–197.
Komori, T., Sakakura, T., Takenaka, Y., Tanaka, K., Okuda, T., 2009. Trineodymium (III) pentairon (III) dodecaoxide, $Nd_3Fe_5O_{12}$. Acta Crystallogr. E 65 (10), i72.
Kosmulski, M., 2018. The pH dependent surface charging and points of zero charge. VII. update. Adv. Colloid Interfac. 251, 115–138.
Kretzschmar, R., Schafer, T., 2005. Metal retention and transport on colloidal particles in the environment. Elements 1 (4), 205–210.
Kulaksız, S., Bau, M., 2013. Anthropogenic dissolved and colloid/nanoparticle-bound samarium, lanthanum and gadolinium in the Rhine River and the impending destruction of the natural rare earth element distribution in rivers. Earth Planet. Sc. Lett. 362, 43–50.
Lachaux, N., Cossu-Leguille, C., Poirier, L., Gross, E.M., Giamberini, L., 2022. Integrated environmental risk assessement of rare earth elements mixture on aquatic ecosystems. Front. Environ. Sci. 10, 974191 https://doi.org/10.3389/fenvs.2022.974191.
Le Jean, M., Montarges-Pelletier, E., Rivard, C., Grosjean, N., Chalot, M., Vantelon, D., Spiers, K., Blaudez, D., 2023. Locked up inside the vessels: rare earth elements are transferred and stored in the conductive tissues of the accumulating fern *Dryopteris erythrosora*. E.S.&T. 57 (7), 2768–2778.
Liang, T., Li, K., Wang, L., 2014. State of rare earth elements in different environmental components in mining areas of China. Environ. Monit. Assess. 186, 1499–1513.
Liang, Y., Yu, D., Jin, J., Xiong, J., Hou, J., Wang, M., Tan, W., 2021. Microstructure of Al-substituted goethite and its adsorption performance for Pb (II) and As (V). Sci. Total Environ. 790, 148202.
Liang, Y., Jin, J., Wei, Z., Wang, M., Xiong, J., Hou, J., Tan, W., 2022. Complexation mechanism of Pb2+ at the ferrihydrite-water interface: the role of Al-substitution. Chemosphere 307, 135627.
Livi, K.J., Villalobos, M., Leary, R., Varela, M., Barnard, J., Villacís-García, M., Midgley, P., 2017. Crystal face distributions and surface site densities of two synthetic goethites: implications for adsorption capacities as a function of particle size. Langmuir 33 (36), 8924–8932.
Ma, M., Gao, H., Sun, Y., Huang, M., 2015. The adsorption and desorption of Ni (II) on Al substituted goethite. J. Mol. Liq. 201, 30–35.
Masue, Y., Loeppert, R.H., Kramer, T.A., 2007. Arsenate and arsenite adsorption and desorption behavior on coprecipitated aluminum: iron hydroxides. Environ. Sci. Technol. 41 (3), 837–842.
Masue-Slowey, Y., Loeppert, R.H., Fendorf, S., 2011. Alteration of ferrihydrite reductive dissolution and transformation by adsorbed As and structural Al: Implications for as retention. Geochim. Cosmochim. Acta 75, 870–886.
Michel, F.M., Ehm, L., Antao, S.M., Lee, P.L., Chupas, P.J., Liu, G., Parise, J.B., 2007. The structure of ferrihydrite, a nanocrystalline material. Science 316 (5832), 1726–1729.
Nakada, R., Tanimizu, M., Takahashi, Y., 2013. Difference in the stable isotopic fractionations of Ce, Nd, and Sm during adsorption on iron and manganese oxides and its interpretation based on their local structures. Geochimica et Cosmochimica Acta 121, 105–119.
Namayandeh, A., Kabengi, N., 2019. Calorimetric study of the influence of aluminum substitution in ferrihydrite on sulfate adsorption and reversibility. J. Colloid Interface Sci. 540, 20–29.
Ni, C., Liu, S., Cui, L., Han, Z., Wang, L., Chen, R., Liu, H., 2016. Adsorption performance of Cr (VI) onto Al-free and Al-substituted ferrihydrites. RSC Adv. 6 (71), 66412–66419.
Ni, C., Liu, S., Wang, H., Liu, H., Chen, R., 2017. Studies on adsorption characteristics of Al-free and Al-substituted goethite for heavy metal ion Cr (VI). Water Air Soil Pollut. 228, 1–10.
Ohta, A., Kagi, H., Nomura, M., Tsuno, H., Kawabe, I., 2009. Coordination study of rare earth elements on Fe oxyhydroxide and Mn dioxides: part I. Influence of a multi-electron excitation on EXAFS analyses of La, Pr, Nd, and Sm. Am. Mineral. 94 (4), 467–475.
Ona-Nguema, G., Morin, G., Juillot, F., Calas, G., Brown, G.E., 2005. EXAFS analysis of arsenite adsorption onto two-line ferrihydrite, hematite, goethite, and lepidocrocite. Environ. Sci. Technol. 39 (23), 9147–9155.
Otero, N., Vitoria, L., Soler, A., Canals, A., 2005. Fertiliser characterisation: major, trace and rare earth elements. Appl. Geochem. 20 (8), 1473–1488.
Pagano, G., Thomas, P.J., Di Nunzio, A., Trifuoggi, M., 2019. Human exposures to rare earth elements: present knowledge and research prospects. Environ. Res. 171, 493–500.
Qin, H.B., Yang, S., Tanaka, M., Sanematsu, K., Arcilla, C., Takahashi, Y., 2021. Scandium immobilization by goethite: Surface adsorption versus structural incorporation. Geochim. Cosmochim. Acta 294, 255–272.
Quinn, K.A., Byrne, R.H., Schijf, J., 2006a. Sorption of yttrium and rare earth elements by amorphous ferric hydroxide: influence of pH and ionic strength. Mar. Chem. 99 (1–4), 128–150.
Quinn, K.A., Byrne, R.H., Schijf, J., 2006b. Sorption of yttrium and rare earth elements by amorphous ferric hydroxide: influence of solution complexation with carbonate. Geochim. Cosmochim. Acta 70 (16), 4151–4165.
Quinn, K.A., Byrne, R.H., Schijf, J., 2007. Sorption of yttrium and rare earth elements by amorphous ferric hydroxide: influence of temperature. Environ. Sci. Technol. 41 (2), 541–546.
Ratié, G., Vantelon, D., Pédrot, M., Beauvois, A., Chaouchi, K., Fosse, C., Davranche, M., 2020. Cerium anomalies in riverbanks: highlight into the role of ferric deposits. Sci. Total Environ. 713, 136544.
Ratié, G., Zhang, K., Iqdal, M., Vantelon, D., Mahé, F., Rivard, M., Komarek, M., Bouhnik-Le, Coz M., Dia, A., Hann, K., Davranche, M., Marsac, R., 2023. Driving forces of Ce (III) oxidation to Ce(IV) onto goethite. Chem. Geol. 633, 121547.
Ravel, B., Newville, M., 2005. ATHENA, ARTEMIS, HEPHAESTUS: data analysis for X-ray absorption spectroscopy using IFEFFIT. J. Synchrotron Radiat. 12 (4), 537–541.
Reddy, L.S., Ko, Y.H., Yu, J.S., 2015. Hydrothermal synthesis and photocatalytic property of β-Ga 2 O 3 nanorods. Nanoscale Res. Lett. 10, 1–7.
Revel, M., Medjoubi, K., Rivard, C., Vantelon, D., Hursthouse, A., Heise, S., 2023. Determination of the distribution of rare earth elements La and Gd in Daphnia magna via micro and nano-SXRF imaging. Environ. Sci-Proc. & Imp. 25 (8), 1288–1297. https://doi.org/10.1039/D3EM00133D.
Rodriguez-Carvajal, J., 1990, July. FULLPROF: A program for Rietveld refinement and pattern matching analysis. In: Satellite Meeting on Powder Diffraction of the XV Congress of the IUCr, vol. 127. Toulouse, France.
Sajih, M., Bryan, N.D., Livens, F.R., Vaughan, D.J., Descostes, M., Phrommavanh, V., Morris, K., 2014. Adsorption of radium and barium on goethite and ferrihydrite: a kinetic and surface complexation modelling study. Geochim. Cosmochim. Acta 146, 150–163.
Santofimia, E., González, F.J., Rincón-Tomás, B., López-Pamo, E., Marino, E., Reyes, J., Bellido, E., 2022. The mobility of thorium, uranium and rare earth elements from Mid Ordovician black shales to acid waters and its removal by goethite and schwertmannite. Chemosphere 307, 135907.
Schwertmann, U., Cornell, R.M., 2000. Iron Oxides in the Laboratory: Preparation and Characterization. John Wiley & Sons.
Schwertmann, U., Taylor, R.M., 1989. Iron oxides. Miner. Soil Environ. 1, 379–438.

Schwertmann, U., Friedl, J., Stanjek, H., Schulze, D.G., 2000. The effect of Al on Fe oxides. XIX. Formation of Alsubstituted hematite from ferrihydrite at 25 degrees C and pH 4 to 7. Clay Clay Miner. 48, 159–172.
Shannon, R.D., 1976. Revised effective ionic radii and systematic studies of interatomic distances in halides and chalcogenides. Acta Crystall. A-Crys. 32 (5), 751–767.
Sherman, D.M., Peacock, C.L., Hubbard, C.G., 2008. Surface complexation of U (VI) on goethite (α-FeOOH). Geochim. Cosmochim. Acta 72 (2), 298–310.
Souza, T.G., Freitas, E.T., Mohallem, N.D., Ciminelli, V.S., 2021. Defects induced by Al substitution enhance As (V) adsorption on ferrihydrites. J. Hazard. Mater. 420, 126544.
Taş, A.C., Majewski, P.J., Aldinger, F., 2002. Synthesis of gallium oxide hydroxide crystals in aqueous solutions with or without urea and their calcination behavior. J. Am. Ceram. Soc. 85 (6), 1421–1429.
Tyler, G., 2004. Rare earth elements in soil and plant systems-a review. Plant Soil 267, 191–206.
U.S. Geological Survey, 1996. Mineral Commodity Summaries 1996. U.S. Geological Survey, p. 198.
U.S. Geological Survey, 2022. Mineral commodity summaries 2022. U.S. Geological Survey, p. 202.
Vantelon, D., Trcera, N., Roy, D., Moreno, T., Mailly, D., Guilet, S., Delmotte, F., Meltchakov, E., Lassalle, B., Lagarde, P., Flank, A.-M., 2016. The LUCIA beamline at SOLEIL. J. Synchrotron Radiat. 23 (2), 635–640.
Villalobos, M., Antelo, J., 2011. A unified surface stuctural model for ferrihydrite: proton charge, electrolyte binding, and arsenate adsorption. Rev. Intern. Contamin. Ambiental 27 (2), 139–151.
Wall, F., 2014. Rare earth elements. Critic. Metals Handb. 312–339.
Wang, Y., Wang, J., Li, P., Qin, H., Liang, J., Fan, Q., 2021. The adsorption of U (VI) on magnetite, ferrihydrite and goethite. Environ. Tech. & Innovation 23, 101615.
Xu, J., Koopal, L.K., Wang, M., Xiong, J., Hou, J., Li, Y., Tan, W., 2019. Phosphate speciation on Al-substituted goethite: ATR-FTIR/2D-COS and CD-MUSIC modeling. Environ. Sci.-Nano 6 (12), 3625–3637.
Xu, T., Catalano, J.G., 2016. Impacts of surface site coordination on arsenate adsorption: macroscopic uptake and binding mechanisms on aluminum hydroxide surfaces. Langmuir 32 (49), 13261–13269.
Zou, J., Tian, H., Wang, Z., 2017. Leaching process of rare earth elements, gallium and niobium in a coal-bearing strata-hosted rare metal deposit—A case study from the late Permian tuff in the Zhongliangshan mine, Chongqing. Metals 7 (5), 174.